JUAN PABLO VASCO CANO

REFLECTIVITY CALCULATIONS IN L3 PHOTONIC CRYSTAL SLAB CAVITIES

REFLECTIVITY CALCULATIONS IN L3 PHOTONIC CRYSTAL SLAB CAVITIES

JUAN PABLO VASCO CANO

ADVISER
Prof. Dr. Paulo Sergio Soares Guimarães
CO-ADVISER
Prof. Dr. Herbert Vinck Posada

Thesis presented to
UNIVERSIDADE FEDERAL DE MINAS GERAIS
as partial requirement for the title of
MASTER IN PHYSICS
Instituto de Ciências Exatas
Departamento de Física

Belo Horizonte, Brasil
January 2013

Juan Pablo Vasco Cano: *Reflectivity calculations in L3 photonic crystal slab cavities,*

SUPERVISORS:

Prof. Dr. Paulo Sergio Soares Guimarães
Departamento de Física
Instituto de Ciências Exatas
Universidade Federal de Minas Gerais
Belo Horizonte, Brasil

Prof. Dr. Herbert Vinck Posada
Departamento de Física
Facultad de ciencias exactas
Universidad Nacional de Colombia
Bogotá, Colombia

LOCATION:
Belo Horizonte, Brasil

. . . to my loved ones, who have supported me during this difficult but rewarding career.

ABSTRACT

In this work, a detailed study is made of the reflectivity spectrum of L3 photonic crystal slab cavities. The scattering matrix method for patterned multilayer photonic structures is implemented to study the coupling between the scattering and bounded states in the crystal. Some modifications are made in the original treatment of the method in order to describe arbitrary geometrical shapes of the incident light spot and to calculate the reflectivity in a cross-polarized scheme. The lineshape of the fundamental mode resonance is well fitted by the Fano formula, evidencing an electromagnetic Fano interference phenomenon in the reflection process. It is found that the lineshape of the Fano resonance can be accurately controlled and reversed by the polarization of the incident field, and the continuum contribution in the Fano phenomenon can be enhanced increasing the incident spot size. Good agreement is obtained between the theoretical and experimental results.

The outline of the work is as follows: Chapter one presents a general state of the art in the photonic crystal area. Then, in chapter two, the fundamental concepts of the solid state physics and electromagnetism in inhomogeneous and periodic media are described. In chapter three a revision is made of the standard plane wave expansion method applied to two dimensional photonic crystals. In chapter four the scattering matrix treatment of patterned multilayer structures is formulated in a general form, to study the diffractive properties of photonic structures. Chapter five presents the implementation of the scattering matrix method to photonic crystal slabs and in chapter six the principal results of this work are presented and discussed. Finally, chapter seven contains the principal conclusions and perspectives.

RESUMO

Neste trabalho é feito um estudo detalhado do espectro de refletividade de cavidades L3 em cristais fotônicos. O método de matriz de espalhamento aplicado a estruturas fotônicas multicamadas é implementado para estudar o acoplamento entre os estados dispersados e confinados pelo cristal. Algumas modificações são feitas no tratamento inicial do método, a fim de descrever geometrias arbitrárias do feixe de luz incidente e calcular a refletividade em um esquema de polarização cruzada. A forma de linha da ressonância do modo fundamental é bem ajustada pela fórmula de Fano, evidenciando um fenômeno de interferência de Fano eletromagnético no processo de reflexão. Verifica-se que a ressonância de Fano pode ser sintonizada com precisão via a polarização do campo incidente. Demonstra-se ainda que a importância relativa das contribuições da componente contínua e da componente discreta na interferência de Fano pode também ser controlada através da variação do tamanho do feixe incidente. Um bom acordo é obtido entre os resultados teóricos e experimentais.

O esboço do trabalho é o seguinte: O Capítulo 1 apresenta o estado geral da arte na área de cristais fotônicos. Em seguida, no Capítulo 2, são descritos os conceitos fundamentais da física do estado sólido e eletromagnetismo em meios heterogêneos e periódicos. No Capítulo 3 é feita uma revisão do método padrão de expansão em ondas planas aplicado a cristais fotônicos de duas dimensões. No Capítulo 4, o tratamento de matriz de espalhamento para estruturas fotônicas multicamadas é formulado de uma forma geral para estudar as propriedades de difração de estruturas fotônicas. O Capítulo 5 apresenta a implementação do método de matriz de espalhamento a lâminas de cristal fotônico e no Capítulo 6, os principais resultados deste trabalho são apresentados e discutidos. Finalmente, o Capítulo 7 contém as principais conclusões e perspectivas.

PUBLICATIONS

1. P.T. Valentim, I.J. Luxmoore, D. Szymanski, J.P. Vasco, H. Vinck-Posada, P.S.S. Guimarães, D.M. Whittaker, A.M. Fox and M.S. Skolnick, "Fano Resonance in GaAs 2D Photonic Crystal Nanocavities", *AIP Conf. Proc.* no. 1399, pp. 1013-1014, 2011.

2. P.T. Valentim, J.P. Vasco, I.J. Luxmoore, D. Szymanski, H. Vinck-Posada, A.M. Fox, D.M. Whittaker, M.S. Skolnick, and P.S.S. Guimarães, "Asymmetry tuning of Fano resonances in GaAs photonic crystal cavities", *Submitted to Applied Physics Letters*.

3. J.P. Vasco, P.T. Valentim, H. Vinck-Posada, and P.S.S. Guimarães, "Fano resonances in L3 photonic crystal slab cavities", *To be Submitted for publication*.

AGRADECIMIENTOS

Primero que todo quiero agradecer especialmente a mi orientador Paulo Sergio por su acompañamiento durante mi proceso de formación como investigador. Su confianza y apoyo fueron claves en el desarrollo de este trabajo. Al profesor y gran amigo Herbert Vinck por su constancia y valiosas discusiones, que tornaron en repetidas ocasiones los panoramas complejos en sus contrapartes más simples.

Agradezco a CNPq, FAPEMIG, CAPES y al INCT-DISSE por su financiamento durante mi maestría, que fue esencial para la fina- lización de esta tesis.

Finalmente, agradezco de corazón a todos aquellos que me acompañaron, motivaron y brindaron su apoyo durante mi maestría. Ellos también hacen parte de este trabajo!

CONTENTS

Part I

PRELIMINARY CONCEPTS

1 STATE OF THE ART

The first studies in photonic structures, performed by Lord Rayleigh in one-dimensional crystals [1], go back to the year 1887. Rayleigh found that it is possible to obtain angular regions where the light is partially or totally reflected when the incident angle is changed; besides this, the reflection occurs only for some colors or wavelengths which are complementaries to the set of colors transmitted. These regions of high reflectivity were called, one century latter, stop bands or photonic band gaps. Subsequent studies made in the decade of 1970 by Bykov show the effect of the photonic band gap in the spontaneous emission rate of active samples embedded into one-dimensional crystals [2]. Nevertheless, it was only in the year 1987 with the works of Yablonovitch and John [3, 4], that the concept and the name of "photonic crystal" were well established: photonic crystals are systems whose dielectric function is periodic in space. The main idea proposed by Yablonovitch was to use three-dimensional crystals with the goal of controlling the spontaneous emission rate through a suitable engineering of the electromagnetic density of states. At the same time, John proposed ways to induce light localization and its control in such systems.
The revolutionary works of Yablonovitch and John led to an explosion of publications in the field which, from that moment on, have had an exponential growth until now. The extraordinary properties of photonic crystals and their effects on the electromagnetic flux radiation make them promising systems for many applications in physics and technology. Some of these are briefly showed and explained in the following sections.

1.1 HIGH-Q PHOTONIC CRYSTAL CAVITIES

The study of light interaction with matter in solid state cavity systems has become very important in the recent years due to their potential applications in fundamental physics, solid state lasers and quantum information. Based on cavity quantum electrodynamics (C-QED), the key parameters responsible for the enhancement of spontaneous emission rates of the emitters (quantum dots for example) are the quality factor Q and the modal volume V. This enhancement phenomenon known as Purcell effect is determined by the fraction Q/V. Therefore, it is important to build cavities with high Q and low V to attain strong coupling between the emitter and the cavity

mode. There are several types of nanocavities proposed in the literature. The main ones [5] are micropillars, microdisks and photonic crystals. Of these, photonic crystal cavities, which are point defects in a regular photonic crystal, are promising systems to achieve this purpose. These cavities can have high quality factors and low modal volumes even in the optical regimen, with the benefit that they can be embedded in a solid state system, enabling the insertion of emitters as quantum dots. There are many works focused in the optimization of the fraction Q/V in photonic crystal cavities through small perturbations of their geometrical parameters. Figure 1 shows the results obtained for the Q optimization in a photonic crystal slab cavity maintaining the modal volume not bigger than 6% of its initial value. The largest values of the quality factor in these calculations have an order of magnitude of 10^5. These results were taken from reference [6].

The enhancement of the spontaneous emission of a light source within a cavity is determined by the Purcell factor, which is proportional to the fraction Q/V. Therefore, the quality factor Q and the modal volume V become very important parameters in the cavity quantum electrodynamics area.

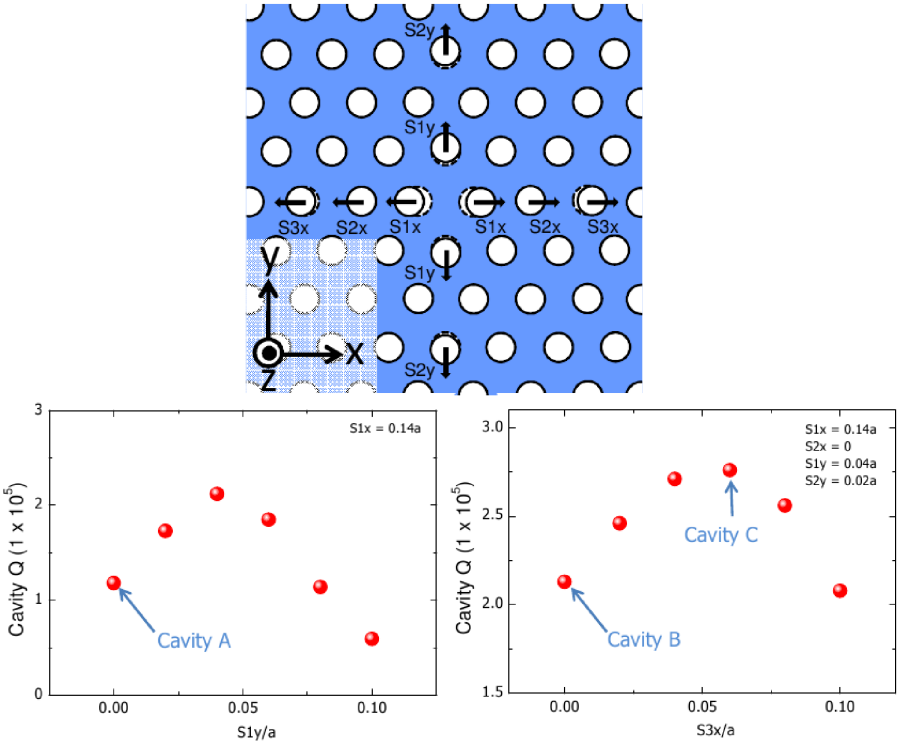

Figure 1: Scheme and results for the Q optimization of a photonic crystal slab cavity. S_{1x}, S_{2x}, S_{3x}, S_{1y} and S_{2y} correspond to the hole shifts. Cavity B and C have a Q factor about twice of the value for cavity A. Taken from reference [6].

One example of application of a photonic crystal is to determine the refraction index of liquid solutions. The basic idea is to immerse the crystal in the sample and the induced change in the background refractive index produces a shift in the resonance frequency of the cavity mode, this shift can be used to characterize the sample. Since the

Q factor is inversely proportional to the width of the transmission peak, the detection limit of such sensors is determined by the quality factor of the cavity. In this way, a higher Q produces a high precision sensor. Figure 2 shows the results obtained for the Q optimization in a nanobeam photonic crystal cavity; there are showed the system and the geometrical parameters (top), the behavior of Q as function of these parameters and the refractive index (bottom-left), the transmission spectrum of the cavity sensing at different sample concentrations and the wavelength mode as function of the refractive index and temperature. These results was taken from reference [7].

The shift induced in the resonance frequency of a photonic crystal cavity by a liquid, in which the crystal was immersed, can be used to determine the refraction index of the liquid. Therefore, the quality factor of the cavity determines a limit in the precision of this sensing.

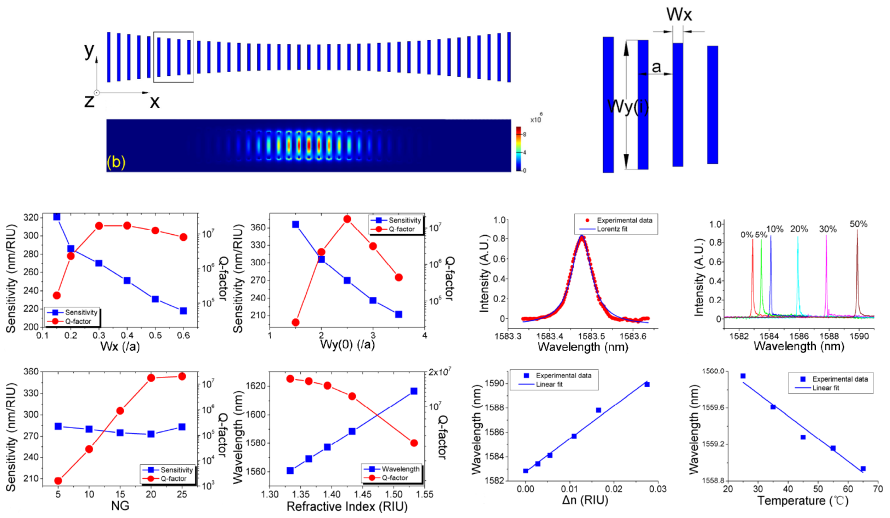

Figure 2: (Top) Scheme of a nanobeam photonic crystal cavity. (Bottom-left) Results for the behavior of Q and sensitivity as functions of the geometrical parameters and the refractive index of the crystal. (Bottom-right) Results for the transmission spectrum of the cavity at different sample concentrations, and its wavelength fundamental mode refractive index and temperature dependences. Taken of the reference [7].

1.2 NONLINEAR PHOTONIC CRYSTALS

By combining several kinds of impurities or defects in photonic crystals, such as waveguides and cavities, it is possible to control the flux of light, and produce photonic crystal circuits or light circuits. However, the all-optical processing of light as a carrier of information can be accomplished only through photonic structures with embedded nonlinear materials [8]. In this way, the nonlinear photonic crystals are essential to create devices such as optical diodes, switches, transistors and gates which will be the fundamental components of an all-optical chip. One of the most important and basic nonlinear phenomena with the capability to produce signal processing in photonic crystals is the bistability; this consists in two states of resonant trans-

mission for the same input signal. To achieve bistability in photonic structures it is necessary to embed a nonlinear material, such as a Kerr-type one which induces a electric field intensity dependence in the refractive index. **??** shows the transmission spectrum of a waveguide bend with three embedded defects made of Kerr-type nonlinear material for two different input powers (left), and the transmission as a function of the input power showing bistability phenomena in the response function of the structure. These results was taken of the reference [8]. Reference [9] is another important work in this topic.

Nonlinear properties of photonic crystal circuits are required to achieve all-optical signal processing.

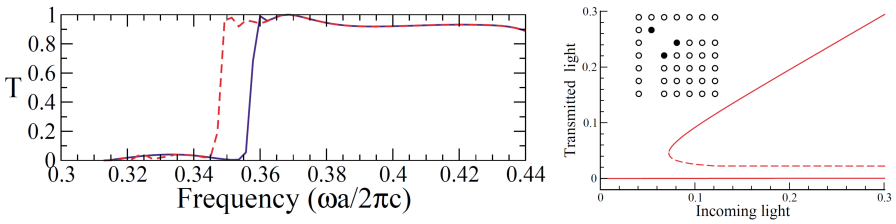

Figure 3: (Left) Transmission spectrum of a waveguide bend with embedded Kerr-type nonlinear material for two different input powers (solid and dashed lines). (Right) Transmitted light as function of the input power showing bistability phenomena. In the diagram of the structure shown in the inset, the black circles represent the Kerr-type materials. Taken of the reference [8].

Since the first works in nonlinear photonic crystals, beginning with Berger [10], there is great interest to obtain efficient all-optical switches and all-optical transistors based in photonic crystals with embedded nonlinear materials. Nozaki *et al.* [11] proposed and built an optical switch which consumes sub-femtojoule energies to operate. The basic principle of operation is based in the nonlinear properties of the cavity material used in the system. Figure 4 shows the scheme of the photonic switch; the pump power has the function to control the resonance frequency of the H0 nanocavity and determine the states "off" and "on" of the switch: when there is an input pump power the refractive index of the cavity increases, then the resonance frequency decreases and the wavelength increases consequently. Therefore, as is showed in the bottom-left of the Figure (dashed lines), the transmission goes to zero and the signal is not transmitted. When there is not an input pump power, the resonance frequency of the cavity coincides with the frequency of the input signal and therefore it is transmitted. In the bottom-right, the intensity distribution of the fundamental H0 mode, which has a very low modal volume, is shown. An interesting work in which an optical transistor based in the all-optical switching is studied, is discussed in the reference [12].

With the possibility of all-optical switching it is reasonable to think in all-optical logic gates, which will be the fundamental constituents of

all-optical microprocessors chips. Figure 5, taken of the reference [13], shows the schematization of an all-optical gate in a photonic crystal slab (top-right) based on the same idea of the all-optical switching shown in Figure 4. The two cavities shown in Figure 5 are made of nonlinear materials. The table of the Figure 5 shows the principles of the gates AND, NAND, OR and NOR in this all-optical system.

All-optical switching is the basic principle of operation of all-optical transistor and logic gates, which will be the fundamental components of an all-optical microprocessor.

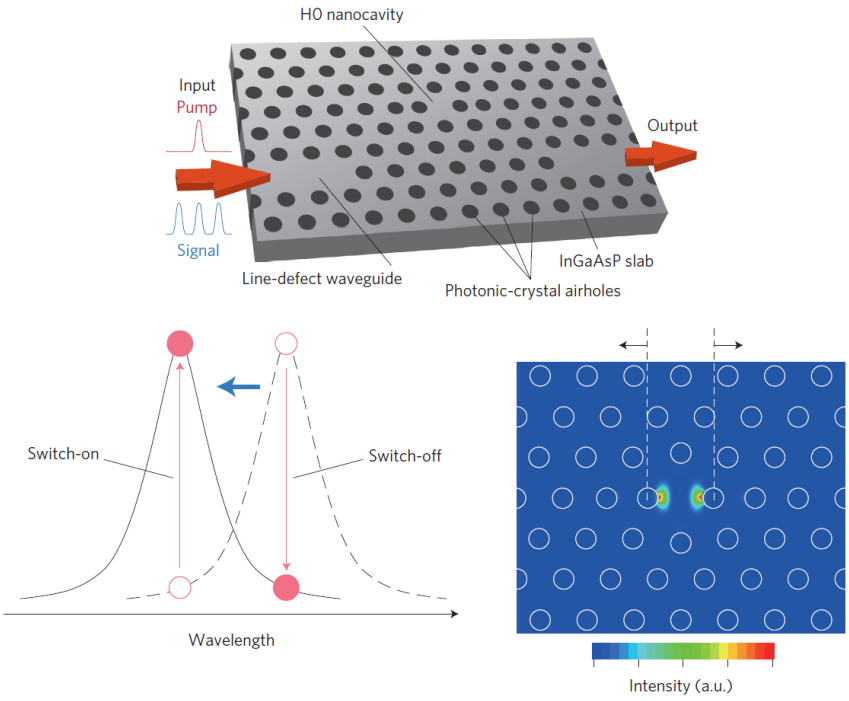

Figure 4: (Top) Structure of the photonic crystal switch; the input pump controls the states "off" and "on" of the switch, determining a zero or total transmission of the signal, respectively. (Bottom-left) Principle of operation of the switch. (Bottom-right) Intensity distribution of the fundamental Ho cavity mode. Taken of the reference [11].

For the gate AND, the fundamental resonances of the two cavities are f_1 and f_2 respectively, with the condition $f_1 = f_2$. The initialization is $f_1 \neq f_0$, where f_0 is the frequency of the input signal. There are two normally incident pump lights I_1 and I_2 associated to the logic states. When there is only I_1 the power is not sufficient to shift the resonance of f_1 to f_0 ($f_1 \neq f_0$), and the signal is not transmitted (logic 0). When there is only I_2 the results is also $f_2 \neq f_0$ (logic 0), however, when there are I_1 and I_2 the power is sufficiently high to make $f_1 = f_0$, and the signal is totally transmitted (logic 1). The principles of the other gates NAND, OR and NOR share the same idea.

1.3 FANO RESONANCES AND THEIR APPLICATIONS

Fano interference is a universal phenomenon that occurs in many physical systems. It is produced when an interference between a dis-

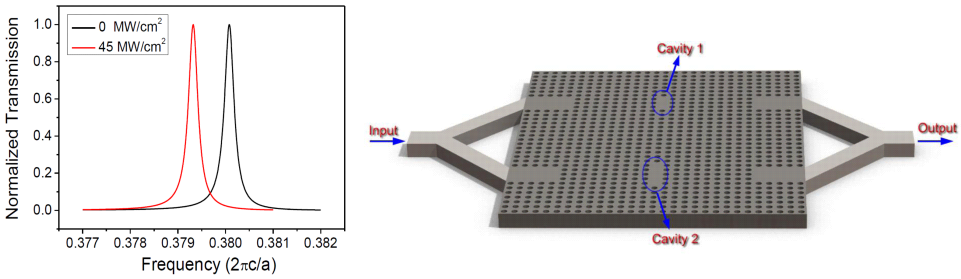

The principles of all-optical AND, NAND, OR, and NOR gates

Logic gate	Initialization	I_1	I_2	I_1 & I_2
AND ($f_1 = f_2$)	$f_1 \neq f_0$ logic 0	$f_1 \neq f_0$ logic 0	$f_1 \neq f_0$ logic 0	$f_1 = f_0$ logic 1
NAND ($f_1 \neq f_2$)	$f_2 = f_0$ logic 1	$f_1 = f_0$ logic 1	$f_1 = f_0$ logic 1	$f_1 \neq f_0, f_2 \neq f_0$ logic 0
OR ($f_1 \neq f_2$)	$f_1 \neq f_0, f_2 \neq f_0$ logic 0	$f_2 = f_0$ logic 1	$f_2 = f_0$ logic 1	$f_1 = f_0$ logic 1
NOR ($f_1 = f_2$)	$f_1 = f_0$ logic 1	$f_1 \neq f_0$ logic 0	$f_1 \neq f_0$ logic 0	$f_1 \neq f_0$ logic 0

Figure 5: (Top-left) Nonlinear response of the cavity resonance to the power of the pump light. (Top-right) Diagram of the all-optical gates based in a photonic crystal structure. (Bottom) Principles of all-optical gates AND, NAND, OR, and NOR. Taken of the reference [13].

crete state and a continuum of states takes place. Usually, in defective photonic crystals, the discrete state is determined by the resonance of a cavity, and the continuum of states are determined by a waveguide or by the external environment (when there is a finite thickness of the crystal). Fano resonances are characterized by having an asymmetrical sharp peak which varies the response function of the system in a range narrower than the full width of the resonance itself. In photonic crystals this response function is typically the transmission function of the crystal. When nonlinear materials are involved, Fano resonances have the capability of increasing significantly the contrast between the two stable states in bistability phenomena [14]. In the reference [15] an all-optical diode with ultrahigh contrast ratio induced by Fano resonances is studied. The basic idea, which is shown in Figure 6 (top-left), is to take advantage of the asymmetry shape of the Fano resonance to increase the transmission contrast ratio defined as $C(I_i) = I_{RL}/I_{LR}$, where I_i is the incident intensity, I_{RL} is the transmitted intensity in the right to left direction and I_{LR} is the transmitted intensity in the left to right direction. This ratio is low for Lorentzian resonances lineshapes. The solid lines represents the linear transmissions and the dashed lines represent the nonlinear transmissions (dash-dotted: right to left and dashed: left to right) for the Lorentzian-shape (left) and Fano-shape (right) spectrums. In the bottom-left of the Figure 6 is shown the structure, where C_1 and C_2

are the nonlinear cavities. The intensities of the RL and LR regimes as well as the contrast ratio are shown in the top-right, and the electric field distributions are shown in the bottom-right. Clearly the contrast is high between the two operating states.

The asymmetric sharp peak of Fano resonances produces a very high variation in the transmission function of the photonic structure in a range narrower than the full width of the resonance itself.

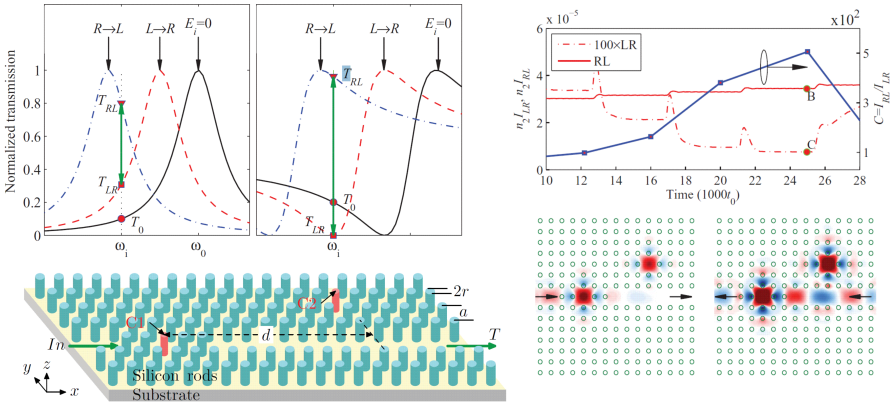

Figure 6: (Top-left) Comparison between Lorentzian-shape and Fano-shape spectrums for the linear (solid line) and nonlinear regimes (dash-dotted and dashed lines): ω_0 is the frequency of the linear resonance, ω_i is the frequency of operation, T_{RL} and T_{LR} are the transmissions for the two operating states right to left and left to right respectively. (Bottom-left) Scheme of the photonic structure, C_1 and C_2 are the nonlinear cavities. (Top-right) I_{RL}, I_{LR} and $C(I_i)$ as functions of time. (Bottom-right) Electric field distributions in the two operating states of the diode. Taken of the reference [15].

1.4 QUANTUM WELL INFRARED PHOTODETECTORS

Quantum well infrared photodetectors (QWIPs) have become very important for infrared detection in the mid-infrared. One problem with this type of detector is the fact that it is not sensitive to normally incident radiation since the intra-band transitions which are responsible for the detection couple only to the component of the electric field perpendicular to the quantum wells. The usual solution for this is to illuminate at non-zero incident angle or fabricate a diffraction grating on top of the detector, which produces an electric field component in the perpendicular direction [16, 17]. Nevertheless, there is another interesting approach: insert the active region of the detector, i.e., the quantum wells, inside a photonic crystal slab optimized for the desired detection wavelength. An extra important advantage of this is that the absorption of the infrared radiation is enhanced through a resonant coupling. This is possible since photonic crystal slabs support modes with non-zero perpendicular electric field component, which can be excited by a normal incident plane wave. Figure 7 shows the principal results of the work described in detail in reference [18]. The top shows the system, which consists of a quan-

tum well photodetector embedded in a photonic crystal slab. The first order mode have its electric field highly concentrated in the center of the structure (photodetector region). In bottom the results for the detectivity, detectivity enhancement and signal enhancement are shown with respect to the standard QWIP (illuminated at 45°). The photonic crystal slab quantum well infrared photodetector (PCS-QWIP) can be 20 times more efficient than the standard QWIP.

Photonic crystal slabs can be used to enhance the absorption in quantum well infrared photodetector through a resonant coupling with the crystal modes.

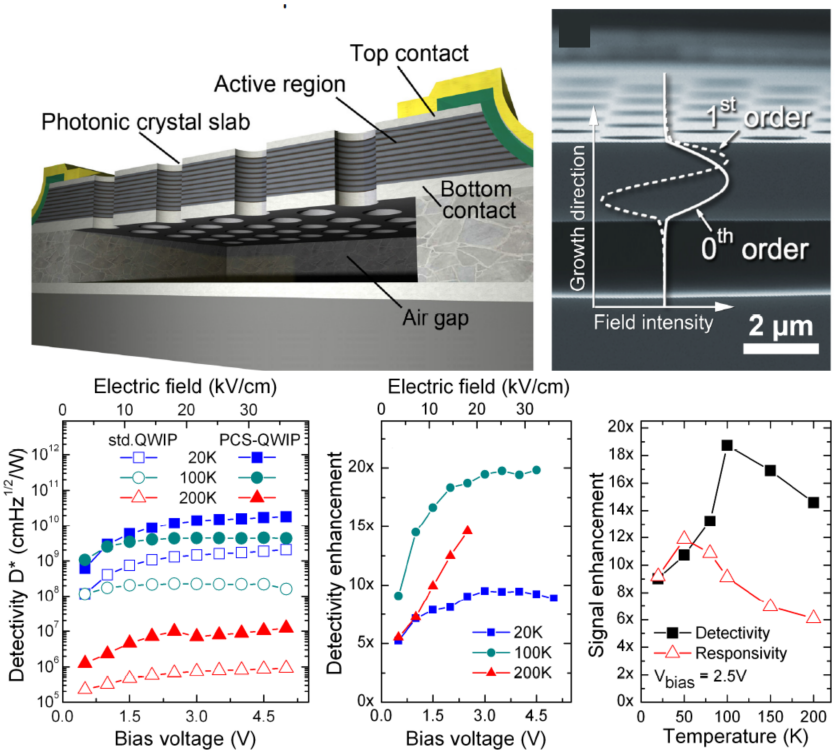

Figure 7: (Top) Photonic crystal slab quantum well infrared photodetector (PCS-QWIP), the first order mode is highly concentrated in the center of the slab, which is the QWIP region. (Bottom) Results for the detectivity, detectivity enhancement and signal enhancement with respect to the standard QWIP. Taken of the reference [18].

1.5 SUMMARY

In this chapter, some applications of photonic crystals have been overviewed. Quantum well infrared photodetectors is the most promissing application, due to the possibility of mass production and the advantages gained in performance. In the following chapter, the fundamental concepts of the solid state physics and electromagnetism in inhomogeneous and periodic media are described. A review of these concepts is essential to understand the basic theory of photonic crystals.

2

FUNDAMENTAL THEORY

When a wave propagates in a dispersion medium, it undergoes multiple scattering if the wavelength involved is comparable with the size of the scatterers. In particular, the electrons or electron waves undergo multiple scattering in periodic arrays of atoms or atomic crystals. Constructive interference between the electronic waves originates allowed electronic states as valence and conduction bands, on the other hand, destructive interference originates forbidden electronic states. The allowed electronic energies are represented by bands and the forbidden ones by electronic band gaps. Analogously, the photons or electromagnetic waves undergo multiple scattering in periodic arrays of dielectrics. A material in which there is a periodic variation of the dielectric function, with period that is of the same order of magnitude of the wavelength involved, is usually called a photonic crystal. In the same manner as for an atomic crystal, in a photonic crystal constructive interference originates bands or allowed states and destructive interference originates photonic band gaps or forbidden states. In this way, the physical origin of the photonic band gaps and the electronic band gaps is, in essence, the same: interference phenomena produced by multiple scattering in a medium with a periodic distribution of scatterers. Whereas the electronic band gaps are produced in atomic crystals, the photonic band gaps are produced in photonic crystals. Therefore, it is expected that a large number of features that characterize atomic crystals are inherited by photonic crystals, such as Bravais lattices, primitive cells, Brillouin zones, energy bands, impurity bands and Bloch states. Nevertheless, there are important differences: the electron dynamics is governed by the scalar Schrödinger equation, whilst the electromagnetic dynamics is governed by the fully vectorial Maxwell equations. Another important difference is related with the statistical nature of the electrons; since electrons are fermions the interactions electron-electron are relevant in atomic crystals, in contrast to photon-photon interactions, which at typical energies in photonic crystals can be neglected.

Even though in photonic crystals literature the word photon is widely used, the emergence of band gaps can be explained through a classical treatment of the Maxwell equations in materials with a periodic refractive index. It is important to mention that the principal characteristic of photonic crystals is their capability to modify the electromagnetic density of states, which can affect dramatically the radiative

dynamics of active systems immersed in such crystals.

In this chapter a quick review is made of the fundamentals of solid state physics and electromagnetism in inhomogeneous media, theoretical pillars in the study of photonic crystals.

2.1 FUNDAMENTALS OF SOLID STATE PHYSICS

The characterization of the electronic states in atomic crystals is addressed in the solid state physics. In this way, a mathematical and physical understanding of the concepts underlying their methods and interpretations is of great importance to embark the study of the physical mechanisms that characterize the photonic states in periodic media.

Bravais lattice

In the study of any crystalline solid it is very important the concept of Bravais lattice; this specifies a periodic array in which the basic units of the crystal are organized. Such basic units can be atoms, molecules, or in general, an atomic basis with an arbitrary number of particles. The Bravais lattice contains all the geometrical information about the crystalline structure, without any specification of its composition. Mathematically, a Bravais lattice is defined as all the points of the space whose vector position $\mathbf{R}$ can be written as a linear combination, with integer coefficients, of the primitive lattice vectors $\mathbf{a}_1$, $\mathbf{a}_2$ and $\mathbf{a}_3$:

$$\mathbf{R} = n_1\mathbf{a}_1 + n_2\mathbf{a}_2 + n_3\mathbf{a}_3. \tag{1}$$

It is said that the vectors $\mathbf{a}_1$, $\mathbf{a}_2$ and $\mathbf{a}_3$ generate or expand the crystal lattice, and the vector $\mathbf{R}$ is called the lattice vector.

Primitive cell

That portion of volume, area or length, which fills the space under translations of the lattice vector, without overlapping of neighboring portions, is known as the primitive cell or primitive unit cell of the lattice. A primitive cell contains only one lattice point, therefore, if n is the point density and v the volume, it must fulfill $nv = 1$, however this cell is not unique, and it can be constructed of several ways for a given lattice. It is possible to construct a primitive cell, with the symmetry properties of the lattice, choosing an arbitrary lattice point and drawing lines from it to its first neighbors, the space enclosed by the planes perpendicularly bisecting these lines determines such cell which is known as the Wigner-Seitz cell.

Reciprocal lattice and Brillouin zone

Given a arbitrary plane wave $e^{i\mathbf{k}.\mathbf{r}}$ and a Bravais lattice described by a lattice vector $\mathbf{R}$, it is possible to choose a set of $\mathbf{G}$ vectors which make the plane wave inherit the periodicity of the lattice. the set of $\mathbf{G}'s$ determine a lattice known as the reciprocal lattice, which is the Bravais lattice in k or Fourier space. Mathematically, the reciprocal lattice is defined as:

$$e^{i\mathbf{G}\cdot(\mathbf{r}+\mathbf{R})} = e^{i\mathbf{G}\cdot\mathbf{r}}. \tag{2}$$

Since the reciprocal lattice is another Bravais lattice, in the same way as in real space, the reciprocal primitive lattice vectors $\mathbf{b}_1$, $\mathbf{b}_2$ and $\mathbf{b}_3$ are defined as the vectors which expand such lattice, and the reciprocal lattice vector as a linear combination, with integer coefficients, of the primitive vectors:

$$\mathbf{G} = m_1\mathbf{b}_1 + m_2\mathbf{b}_2 + m_3\mathbf{b}_3. \tag{3}$$

The Wigner-Seitz cell of the reciprocal space is known as the first Brillouin zone. The vectors in the real and reciprocal space are related through the following expressions:

$$\mathbf{b}_i \cdot \mathbf{a}_j = 2\pi\delta_{ij}, \qquad \mathbf{G}\cdot\mathbf{R} = 2\pi l, \tag{4}$$

where l is an integer number.

Bloch's theorem

Bloch's theorem states [19]: *The eigenstates ψ of the one-electron Hamiltonian $H = -\hbar^2\frac{\nabla^2}{2m} + U(\mathbf{r})$, where $U(\mathbf{r}+\mathbf{R}) = U(\mathbf{r})$ for all $\mathbf{R}$ is a Bravais lattice, can be chosen to have the form of a plane wave times a function with the periodicity of the Bravais lattice*:

In the theory of ordinary differential equations an equivalent form of the Bloch theorem is called the Lyapunov-Floquet theorem.

$$\Psi_{n\mathbf{k}}(\mathbf{r}) = e^{i\mathbf{k}\cdot\mathbf{r}}u_{n\mathbf{k}}(\mathbf{r}). \tag{5}$$

Where n is the band number, $\mathbf{k}$ is the wave vector and $u_{n\mathbf{k}}(\mathbf{r})$ is a periodic function with the periodicity of the Bravais lattice: $u_{n\mathbf{k}}(\mathbf{r}+\mathbf{R}) = u_{n\mathbf{k}}(\mathbf{r})$. The eigenstate of expression (5) is called a Bloch state. The Bloch states are subject to the boundary condition:

$$\Psi_{n\mathbf{k}}(\mathbf{r}+\mathbf{R}) = e^{i\mathbf{k}\cdot\mathbf{R}}\Psi_{n\mathbf{k}}(\mathbf{r}). \tag{6}$$

For all $\mathbf{R}$ in a Bravais lattice. The condition (6) is known as the Bloch boundary condition.

Energy bands

The problem to find the eigenvalues of the time independent Schrödinger equation for an electron in periodic potentials is the same problem to

find the energy function $E(\mathbf{k})$, which is the dispersion relation or the energy bands of the electron in the atomic crystal. Since the reciprocal lattice is a Bravais lattice, the dispersion relation can be parametrized translating the function $E(\mathbf{k})$ to the first Brillouin zone, subtracting from $\mathbf{k}$ the appropriated reciprocal vector. The equivalents vectors $\mathbf{k}$ and $\mathbf{k}+\mathbf{G}$ corresponds to the same point in this zone, however $E(\mathbf{k}) \neq E(\mathbf{k}+\mathbf{G})$. Therefore, it is convenient to introduce a new index n, known as the band index, to represent the values of $E(\mathbf{k})$ associated to each translation of $\mathbf{k}$ to the first Brillouin zone from the another ones. Being n the band index, $E_n(\mathbf{k})$ is the correct form to represent the energy for one electron with a wave vector $\mathbf{k}$ in the first Brillouin zone. This convention which indexes the electron energies is known as the reduced scheme zone.

2.2 FUNDAMENTALS OF ELECTROMAGNETISM

The electromagnetic states in a photonic crystal are governed by the wave equation in inhomogeneous media, which can be written as an eigenvalue problem whose differential operator is Hermitian. This fact is of great importance, since most of the quantum mechanical theory of observables can be directly applied in the characterization of the photonic crystal through a fully treatment. In this way, the theory of photonic crystals takes advantage of the methods used in quantum mechanics to describe the scattering dynamics of classical electromagnetic fields in periodic media. See for example the reference [20].

Since photonic crystals are dielectric systems, their physical properties are described by the electromagnetic theory.

Maxwell equations and wave equation

The electromagnetic field dynamics is described by the Maxwell equations which in MKS units, when free charges and electric currents are absent, take the form:

$$\begin{aligned}
\nabla \cdot \mathbf{D}(\mathbf{r}, t) &= 0, \\
\nabla \cdot \mathbf{B}(\mathbf{r}, t) &= 0, \\
\nabla \times \mathbf{E}(\mathbf{r}, t) &= -\frac{\partial}{\partial t}\mathbf{B}(\mathbf{r}, t), \\
\nabla \times \mathbf{H}(\mathbf{r}, t) &= \frac{\partial}{\partial t}\mathbf{D}(\mathbf{r}, t).
\end{aligned} \tag{7}$$

Where $\mathbf{E}$, $\mathbf{H}$, $\mathbf{D}$ and $\mathbf{B}$ are the electric, magnetic, electric displacement and magnetic induction fields respectively. The fields $\mathbf{H}$ and $\mathbf{B}$, and $\mathbf{E}$ and $\mathbf{D}$ are related by the known constitutive relations [21]. In the usual treatment of photonic crystals nonmagnetic materials are considered, therefore, the magnetic permeability of the medium is the same as for the free space, and the constitutive relation between $\mathbf{H}$ and $\mathbf{B}$ is written as:

$$\mathbf{B}(\mathbf{r}, t) = \mu_0 \mathbf{H}(\mathbf{r}, t). \tag{8}$$

The dielectric function of the medium will be assumed real, isotropic and frequency independent. In this way, if ϵ_0 is the dielectric constant of vacuum and $\epsilon(\mathbf{r})$ is the relative dielectric function of the medium, the constitutive relation between $\mathbf{E}$ and $\mathbf{D}$ is written as:

$$\mathbf{D}(\mathbf{r}, t) = \epsilon_0 \epsilon(\mathbf{r}) \mathbf{E}(\mathbf{r}, t). \tag{9}$$

Replacing the relations (8) and (9) in the equations (7), the Maxwell equations take the form:

$$\begin{aligned}
&\nabla \cdot \epsilon(\mathbf{r}) \mathbf{E}(\mathbf{r}, t) = 0, \\
&\nabla \cdot \mathbf{H}(\mathbf{r}, t) = 0, \\
&\nabla \times \mathbf{E}(\mathbf{r}, t) = -\mu_0 \frac{\partial}{\partial t} \mathbf{H}(\mathbf{r}, t), \\
&\nabla \times \mathbf{H}(\mathbf{r}, t) = \epsilon_0 \epsilon(\mathbf{r}) \frac{\partial}{\partial t} \mathbf{E}(\mathbf{r}, t).
\end{aligned} \tag{10}$$

In order to obtain the relations that govern the propagation of the fields $\mathbf{H}$ and $\mathbf{E}$ independently, equations (10) are decoupled through simple vector identities leading to the electromagnetic wave equations:

$$\nabla \times \frac{1}{\epsilon(\mathbf{r})} \nabla \times \mathbf{H}(\mathbf{r}, t) = -\frac{1}{c^2} \frac{\partial^2}{\partial t^2} \mathbf{H}(\mathbf{r}, t), \tag{11}$$

$$\frac{1}{\epsilon(\mathbf{r})} \nabla \times \nabla \times \mathbf{E}(\mathbf{r}, t) = -\frac{1}{c^2} \frac{\partial^2}{\partial t^2} \mathbf{E}(\mathbf{r}, t), \tag{12}$$

where c, the speed of the light in vacuum, is defined as $\frac{1}{\sqrt{\mu_0 \epsilon_0}}$. In general, $\mathbf{H}$ and $\mathbf{E}$ are complicated functions of space and time. Since the Maxwell equations are linear, it is possible to separate the time and space dependence expanding the fields in a set of harmonic modes. For one harmonic mode the fields become:

$$\begin{aligned}
&\mathbf{H}(\mathbf{r}, t) = \mathbf{H}(\mathbf{r}) e^{-i\omega t}, \\
&\mathbf{E}(\mathbf{r}, t) = \mathbf{E}(\mathbf{r}) e^{-i\omega t}.
\end{aligned} \tag{13}$$

This is not a great limitation because it is known by Fourier analysis that any time dependence in the fields can be described as a suitable combination of this kind of modes. With the expressions (13), the wave equations reduce to:

$$\hat{\Theta} \mathbf{H}(\mathbf{r}) = \nabla \times \frac{1}{\epsilon(\mathbf{r})} \nabla \times \mathbf{H}(\mathbf{r}) = \frac{\omega^2}{c^2} \mathbf{H}(\mathbf{r}), \tag{14}$$

$$\hat{\mathcal{L}}_{\mathbf{E}} \mathbf{E}(\mathbf{r}) = \frac{1}{\epsilon(\mathbf{r})} \nabla \times \nabla \times \mathbf{E}(\mathbf{r}) = \frac{\omega^2}{c^2} \mathbf{E}(\mathbf{r}). \tag{15}$$

In the literature of photonic crystals $\hat{\Theta}$ is called the Maxwell operator.

Eigenvalue problems

The equations (14) and (15) establish ordinary eigenvalues problems with differential operators $\hat{\Theta}$ and $\hat{\mathcal{L}}_{\mathbf{E}}$ respectively. These problems are implicitly dependent on each other, since the fields $\mathbf{H}$ and $\mathbf{E}$ are related through the Maxwell equations. Hence, the solution of any one automatically determines the solution of the other. It is important to mention that the operators $\hat{\Theta}$ and $\hat{\mathcal{L}}_{\mathbf{E}}$ are linear, so that any linear combination of the solutions is also a solution. The key difference between equations (14) and (15) is that $\hat{\Theta}$ is an Hermitian operators, whilst $\hat{\mathcal{L}}_{\mathbf{E}}$ is not. Therefore, the eigenvalue problem (14) is essentially simpler than the problem (15). The Hermiticity of $\hat{\Theta}$ evokes the known spectral theorem of quantum mechanics, which states that the eigenvalues of an Hermitian operator are real and the eigenfunctions of such operator form a basis for the space of states and, for different eigenvalues, are orthogonal [22]. In this way, the following relations are guaranteed:

The analogy between quantum mechanical formalism and the electromagnetic treatment of inhomogeneous media, allows taking advantage of the theoretical methods used in atomic crystals to apply them in photonic crystals.

$$\begin{aligned} &\frac{\omega^2}{c^2} = \left(\frac{\omega^2}{c^2}\right)^*, \\ &\int \mathbf{H}_i^*(\mathbf{r}) \cdot \mathbf{H}_j(\mathbf{r}) d^3\mathbf{r} = N^2 \delta_{ij}. \end{aligned} \tag{16}$$

Where N is a normalization factor. In addition, it is possible to show that for $\epsilon(\mathbf{r}) > 0$, $\hat{\Theta}$ is positive semidefinite, i.e., $\frac{\omega^2}{c^2} \geqslant 0$. Under this condition, the frequencies ω are always real numbers [23].

Variational principle

In analogy to quantum mechanics, the electromagnetic variational principle establishes a connexion between the concentrations and oscillations of the fields (wave functions) in the medium (potential), and the energies associated to these normalized distributions, keeping the orthogonality between the eigenstates of the Maxwell operator. Formally, the variational principle assigns the minimum eigenvalue $\frac{\omega_0^2}{c^2}$, and consequently the mode of lower frequency, to the field $\mathbf{H}_0$ that minimizes the functional:

$$\Phi[\mathbf{H}] = \frac{\int \mathbf{H}^*(\mathbf{r}) \cdot \hat{\Theta}\mathbf{H}(\mathbf{r}) d^3\mathbf{r}}{\int \mathbf{H}^*(\mathbf{r}) \cdot \mathbf{H}(\mathbf{r}) d^3\mathbf{r}}. \tag{17}$$

The functional Φ is known as the Rayleigh-Ritz quotient. The next low frequency mode will minimize Φ within the subspace of functions orthogonal to $\mathbf{H}_0$. The variational expression (17), written in terms of the electric field, takes the form:

$$\Phi[\mathbf{E}] = \frac{\int |\nabla \times \mathbf{E}(\mathbf{r})|^2 \, d^3\mathbf{r}}{\int \epsilon(\mathbf{r}) \, |\mathbf{E}(\mathbf{r})|^2 \, d^3\mathbf{r}}. \tag{18}$$

Expression (18) establishes that the way to minimize the functional Φ is concentrating the electric field in regions of high dielectric dielectric constant and minimizing the spatial oscillations [23].

Electromagnetism in periodic media

When $\epsilon(\mathbf{r}+\mathbf{R}) = \epsilon(\mathbf{r})$, for any $\mathbf{R}$ in a Bravais lattice, the dielectric function represents a photonic crystal or medium with periodic refractive index. The concepts of primitive cell and Wigner-Seitz cell remains unaltered in these arrays whose atomic basis is composed of dielectric materials. The electromagnetic field description is realized through the Bloch theorem, therefore, $\mathbf{E}$ and $\mathbf{H}$ are represented as the product of a plane wave and a periodic function with the periodicity of the lattice. In the same way, the dispersion relation or photonic band diagram $\omega_n(\mathbf{k})$ is constructed in the first Brillouin zone, which can be reduced taking advantage of the symmetry properties of the crystal [1]. A formal treatment about group theory and symmetries in photonic crystals is realized in the reference [24].

1 When the crystal has special symmetry properties, it is possible to reduce the set of independent $\mathbf{k}$ vectors, and consequently reduce the size of the Brillouin zone, obtaining the so called: reduced Brillouin zone.

Part II

SEMI-ANALYTICAL TECHNIQUES

3

PLANE WAVE EXPANSION METHOD

The plane wave expansion method (PWE), or Fourier expansion, exploits the periodicity of the dielectric system to make a periodic expansion of the fields and the dielectric function in a plane wave basis. Such expansion is introduced in equations (14) and (15) to obtain a system of infinite algebraic equations through simple integral orthogonality relations. In principle, any functional basis can be used to expand the fields in photonic crystals [25], however, the plane wave basis is quite simple in their mathematical structure, and makes a very good description of the crystals studied in the present work.

In this chapter a general review is made of the PWE method applied to two-dimensional photonic patterns with infinite thickness. The principal purpose is to give a background for the scattering matrix treatment which is studied in Chapter 4. Studies of photonic crystals with the PWE method can be reviewed in the references [26, 27, 28].

3.1 TWO-DIMENSIONAL PHOTONIC CRYSTAL

A two-dimensional photonic crystal consists of a two-dimensional periodic pattern in a plane (xy plane for example), and a non-periodic or homogeneous pattern in the other dimension. Particularly, here will be studied crystals with general periodic patterns in the xy plane, and a homogeneous distribution in z direction (infinite thickness). Since there is a reflection symmetry plane at any value of z, due to the infiniteness and homogeneity in this direction, the wave vector of the crystal resonances must be totally contained in the plane xy. This fact classifies all the resonances in two distinct polarizations sets or symmetries: transverse electric (TE) and transverse magnetic (TM). The former, in which the electric field is confined to the xy plane, has the non-zero fields components H_z, E_x and E_y. The latter, in which the magnetic field is confined to the xy plane, has the non-zero fields components E_z, H_x and H_y.

TE case

TE modes have electric and magnetic information, consequently any of the equations (14) or (15) can be used to find the solutions. However, the magnetic field wave equation (14) is easier to solve since only one of the magnetic components is different from zero, so that the dimensionality of the magnetic problem is smaller than the electric one.

The fundamental principle of the PWE method is to make an expansion of the all periodical functions in the crystal using a plane wave basis.

Once the component H_z is found, it is possible to find E_x and E_y through Maxwell equations (10). As it was mentioned in Section 2.2, in periodic media H_z can be written as a Bloch state (5):

$$\mathbf{H}(\mathbf{r}) = \hat{\mathbf{z}} H_z(x,y) = \hat{\mathbf{z}} H_z^P(x,y) e^{i\mathbf{k}_{||}\cdot\mathbf{r}}, \tag{19}$$

where $\mathbf{k}_{||} = \hat{\mathbf{x}}k_x + \hat{\mathbf{y}}k_y$ and $H_z^P(x,y)$ is a periodic function with the periodicity of the lattice. There is no dependence in z because the system is homogeneous in this direction. The key of the PWE method is to expand $H_z^P(x,y)$ and $\frac{1}{\epsilon(x,y)}$ in a plane wave basis whose wave vectors determine the reciprocal lattice (2):

$$H_z^P(x,y) = \sum_G C_G e^{i\mathbf{G}\cdot\mathbf{r}}, \tag{20}$$

$$\frac{1}{\epsilon(x,y)} = \eta(x,y) = \sum_G \eta_G e^{i\mathbf{G}\cdot\mathbf{r}}, \tag{21}$$

where $\mathbf{G} = \hat{\mathbf{x}}G_x + \hat{\mathbf{y}}G_y$ is the reciprocal lattice vector (3), and the summation index G indicates a symmetric sum over the all reciprocal vectors $\mathbf{G}$. From expressions (20) and (19), the total magnetic field in z takes the form:

$$\mathbf{H}(\mathbf{r}) = \hat{\mathbf{z}} \sum_G C_G e^{i(\mathbf{G}+\mathbf{k}_{||})\cdot\mathbf{r}}. \tag{22}$$

The expressions (21) and (22) are replaced in equation (14):

$$\begin{aligned}&\nabla \times \sum_{G'} \eta_{G'} e^{i\mathbf{G}'\cdot\mathbf{r}} \nabla \times \hat{\mathbf{z}} \sum_G C_G e^{i(\mathbf{G}+\mathbf{k}_{||})\cdot\mathbf{r}} \\ &= \left(\frac{\omega}{c}\right)^2 \hat{\mathbf{z}} \sum_G C_G e^{i(\mathbf{G}+\mathbf{k}_{||})\cdot\mathbf{r}}.\end{aligned} \tag{23}$$

Considering the following vectorial identities:

$$\begin{aligned}\nabla \times \hat{\mathbf{z}} f(x,y) &= (\hat{\mathbf{x}}\partial_y - \hat{\mathbf{y}}\partial_x) f(x,y), \\ \nabla \times \hat{\mathbf{x}} f(x,y) &= -\hat{\mathbf{z}}\partial_y f(x,y), \\ \nabla \times \hat{\mathbf{y}} f(x,y) &= \hat{\mathbf{z}}\partial_x f(x,y),\end{aligned} \tag{24}$$

the vectorial equation (23) is reduced to the following scalar equation:

$$\begin{aligned}&\sum_{G'G} \eta_{G'} C_G \Big[(G_x + k_x)(G_x' + G_x + k_x) + (G_y + k_y) \times \\ &(G_y' + G_y + k_y)\Big] e^{i(\mathbf{G}'+\mathbf{G})\cdot\mathbf{r}} = \left(\frac{\omega}{c}\right)^2 \sum_G C_G e^{i\mathbf{G}\cdot\mathbf{r}}.\end{aligned} \tag{25}$$

In order to obtain a system of equations in terms of the expansion coefficients, without any spacial dependence, the equation (25) is multiplied by the plane wave $e^{-i\mathbf{G}''\cdot\mathbf{r}}$ and integrated in the orthogonality

region of the plane wave basis RO, which is not necessarily the unit cell [1]. The integrals have the solutions:

$$\int_{RO} e^{i(\mathbf{G}'+\mathbf{G}-\mathbf{G}'')\cdot\mathbf{r}} da = A_{RO}\delta_{\mathbf{G}'+\mathbf{G},\mathbf{G}''},$$
$$\int_{RO} e^{i(\mathbf{G}-\mathbf{G}'')\cdot\mathbf{r}} da = A_{RO}\delta_{\mathbf{G},\mathbf{G}''}. \tag{26}$$

The Kronecker delta functions produced in the integrals (26) simplify the equation (25), leading it to the final expression:

$$\sum_{G} \eta_{\mathbf{G}'-\mathbf{G}} \left[(G_y' + k_y)(G_y + k_y) + (G_x' + k_x)(G_x + k_x)\right] C_G$$
$$= \left(\frac{\omega}{c}\right)^2 C_{G'}, \tag{27}$$

where the result $G_i'' = G_i' + G_i$ obtained in (26) was used, and the dummy index G'' was replaced by G'.

TM case

Taking into account that the only non-zero components of the TM modes are E_z, H_x and H_y, and under the same argument exposed for the TE modes, the solution is obtained for the E_z component through the equation (15). In this way, the electric field can be written as a Bloch state:

Even though the **E** *eigenvalue equation has only one component in the TM case, the eigenvalue problem is not Hermitian, therefore, a slow convergence is expected.*

$$\mathbf{E}(\mathbf{r}) = \hat{\mathbf{z}} \sum_{G} C_G e^{i(\mathbf{G}+\mathbf{k}_{||})\cdot\mathbf{r}}. \tag{28}$$

The function $\frac{1}{\epsilon(x,y)}$ is expanded in the same way as for the previous TE case, and the expressions (21) and (28) are replaced in equation (15):

$$\sum_{G'} \eta_{G'} e^{i\mathbf{G}'\cdot\mathbf{r}} \nabla\times\nabla\times\hat{\mathbf{z}} \sum_{G} C_G e^{i(\mathbf{G}+\mathbf{k}_{||})\cdot\mathbf{r}}$$
$$= \left(\frac{\omega}{c}\right)^2 \hat{\mathbf{z}} \sum_{G} C_G e^{i(\mathbf{G}+\mathbf{k}_{||})\cdot\mathbf{r}}, \tag{29}$$

which is reduced, using the vectorial identities (24), to the following scalar equation:

$$\sum_{G'G} \eta_{G'} C_G \left[(G_x + k_x)^2 + (G_y + k_y)^2\right] e^{i(\mathbf{G}'+\mathbf{G})\cdot\mathbf{r}}$$
$$= \left(\frac{\omega}{c}\right)^2 \sum_{G} C_G e^{i\mathbf{G}\cdot\mathbf{r}}. \tag{30}$$

1 For the hexagonal lattice for example, this region is a rectangle which contains two lattice points. See Appendix A.

At this point, equation (30) is multiplied by $e^{-iG''\cdot r}$, and integrated using the results (26), to obtain the final eigenvalue problem:

$$\sum_G \eta_{G'-G}\left[(G_x+k_x)^2+(G_y+k_y)^2\right]C_G=\left(\frac{\omega}{c}\right)^2 C_{G'}, \qquad (31)$$

where the dummy index G'' was changed to G'.

Note that expressions (27) and (31) are eigenvalue systems of algebraic equations whose eigenvalues are $\left(\frac{\omega}{c}\right)^2$, and whose eigenvectors are determined by the C_G coefficients. The plane wave basis must be truncated in these expressions to solve numerically the problem.

3.2 SUPERCELL APPROACH

When the periodicity of the crystal is broken with defects, it is possible to restore it considering such defects inside a periodic larger cell or supercell.

When an impurity or defect is introduced into the crystal, localized modes can arise in the structure, with energies in the photonic band gap. The rigorous description of defects is made through calculations in finite crystals [29], nevertheless, the complexity involving this kind of studies suggests the introduction of approximations that simplify the problem, maintaining an accurate representation of the system. The supercell approach is one of these approximations. It consists in restoring the periodicity of the crystal considering a bigger "primitive cell", called supercell, with the defect inside it. The complete crystal is built replicating the supercell under translations of the lattice vector in the new Bravais lattice, without overlapping between neighboring supercells. In this manner, the description of the fields in the defective crystals can be made through Bloch states and any method based in this kind of states and the periodicity of the system will be also valid for crystals with defective supercells. If there is a sufficiently large distance between consecutive defects allowing one to neglect the overlapping of their electromagnetic fields, the supercell approach is said to be good. It is important to say that if the magnitude of lattice vector in the supercell is larger, the magnitude of the reciprocal lattice vector becomes shorter in relation to those without supercell considerations (regular lattice). This fact implies a reduction of the Brillouin zone size, and the $\mathbf{k}$ vectors will suffer a higher number of translations in a reduced zone scheme. In this way, the bands associated to the supercell are folded with respect to ones associated to the regular primitive cell, due to the additional translations of $\mathbf{k}$ needed to describe the complete system in a smaller Brillouin zone. To clarify this, suppose a one- dimensional crystal with lattice vector $\mathbf{a}=a\hat{\mathbf{x}}$. From relations (4), the reciprocal lattice vector of $\mathbf{a}$ is $\mathbf{b}=\frac{2\pi}{a}\hat{\mathbf{x}}$, and the Brillouin zone has a size of $\frac{2\pi}{a}$. If the size of the primitive cell is duplicated, i.e., $A=2a$, the associated lattice vector is also duplicated $\mathbf{A}=2\mathbf{a}$, and, consequently, the reciprocal lattice vector of $\mathbf{A}$

will be affected by a factor of one-half, $\mathbf{B} = \frac{1}{2}\mathbf{b}$. The new Brillouin zone has a size of $\frac{\pi}{a}$; so that, the vectors $\mathbf{k}$ lying between $\frac{\pi}{a}$ and $\frac{2\pi}{a}$ becomes linearly dependent to those lying between 0 and $\frac{\pi}{a}$. Therefore, in a reduced zone scheme the bands associated to $\mathbf{k}$ between $\frac{\pi}{a}$ and $\frac{2\pi}{a}$ are translated to the new first Brillouin zone defined between 0 and $\frac{\pi}{a}$, producing an apparent folding of the bands with respect to the crystal with regular primitive cell. For more details consult reference [30].

3.3 IMPLEMENTATION

The general features of the PWE method have been described above. Technical details of its implementation to non-defective and defective two-dimension photonic crystals of square and hexagonal lattices can be consulted in the reference [31].

4

SCATTERING MATRIX METHOD

The scattering matrix method (SMM) is a powerful tool to solve the problem of the scattering by a large finite number of objects. Basically, the method studies the individual scattering by each object and then evaluates the coupling phenomena between them. Even though the treatment of the electromagnetic fields in the SMM is quite rigorous, it is based on an intuitive physical idea: the fields scattered by the structure are causally related with the fields incident in it. In the photonic crystal area, the SMM has been used to solve the scattering properties of finite two-dimensional periodic arrays of cylinders, ellipses and squares [29, 32, 33]. Nevertheless, such scattering objects have an infinite length in the non-periodic direction, which is a great limitation to study photonic crystals with finite thickness, known as photonic crystal slabs. To overcome this difficulty Whittaker and Culshaw [34] proposed a new approach: they solve the problem transferring the infiniteness in the perpendicular direction of the periodic pattern to the extent of the pattern itself. In this way, the photonic structure consists of a multilayer system with periodic infinite patterns perpendicular to the layer growth direction. Each layer has a finite thickness and represents a complex scattering object which couples to the other ones. Initially, the scattering matrix treatment of this kind of systems was applied by Ko and Inkson [35] to solve the electron tunneling in multilayer semiconductor heterostructures; the work [34] is nothing more than the electromagnetic equivalent formulation for photonic structures.

The scattering matrix treatment applied to multilayer photonic structures can be summarized as follows: the band structure is solved in each layer to describe the states in the direction perpendicular to the pattern as simple plane waves; these states are used to represent the electromagnetic field in terms of forward and backward propagating waves; the scattering matrix is calculated using this representation, and finally, the problem is completely solved applying the boundary conditions of the electric and magnetic fields in each interface of the multilayer system. Once the scattering matrix is obtained, it is possible to relate the outgoing waves to the incoming ones in the structure, which allow the calculation of diffractive properties as the reflection and transmission.

In this chapter the main aspects of the method, which is developed in detail in the original work of Whittaker, are presented. Some new

contributions are made in the description of the incident field and the calculation of the reflectivity.

4.1 MAXWELL EQUATIONS IN THE MOMENTUM REPRESENTATION

If a time harmonic dependence is considered for the fields (as it was discussed in Section 2.2), the electric field is rescaled as $\omega\epsilon_0\mathbf{E} \to \mathbf{E}$ and the frequency is rescaled as $\sqrt{\mu_0\epsilon_0}\omega = \omega/c \to \omega$, the Maxwell curl equations (10) take the following form:

$$\begin{aligned}\nabla \times \mathbf{H}(\mathbf{r}_{||}, z) &= -i\epsilon(\mathbf{r}_{||}, z)\mathbf{E}(\mathbf{r}_{||}, z),\\ \nabla \times \mathbf{E}(\mathbf{r}_{||}, z) &= i\omega^2\mathbf{H}(\mathbf{r}_{||}, z),\end{aligned} \tag{32}$$

where the z dependence has been made completely explicit. The equation $\nabla \cdot \mathbf{E} = 0$ is automatically satisfied in the curl equation of $\mathbf{H}$, and $\nabla \cdot \mathbf{H} = 0$ is satisfied if the expansion of $\mathbf{H}$ is made in a zero divergence basis. Since the layers of the system are composed by photonic structures, the magnetic and electric fields in each layer can be written as Bloch states:

$$\begin{aligned}\mathbf{H}(\mathbf{r}_{||}, z) &= \sum_{\mathbf{G}} \widetilde{\mathbf{H}}_{\mathbf{k}_{||}}(\mathbf{G}, z) e^{i(\mathbf{k}_{||}+\mathbf{G})\cdot\mathbf{r}_{||}},\\ \mathbf{E}(\mathbf{r}_{||}, z) &= \sum_{\mathbf{G}} \widetilde{\mathbf{E}}_{\mathbf{k}_{||}}(\mathbf{G}, z) e^{i(\mathbf{k}_{||}+\mathbf{G})\cdot\mathbf{r}_{||}}.\end{aligned} \tag{33}$$

Note that the periodic pattern is contained in the xy plane, and the growth direction of the structure is z. The expressions (33) are more general than the (22) and (28) ones, since the expansion coefficients, and consequently the fields, have a functional dependence in z. The explicit reciprocal lattice vector $\mathbf{G}$ is also considered in the functional dependence of the expansion coefficients and in the summation index, which is different from Section 3.1 where only the magnitude of $\mathbf{G}$ was written to specify the indexes; this is made with the purpose to use a more appropriate notation in the mathematical developments discussed below.

The fields can be represented as column vectors whose components correspond to their Fourier coefficients in the expansions (33), and the dielectric function as a square matrix populated by its expansion coefficients in a plane wave basis:

$$\begin{aligned}\mathbf{h}(z) &= \left[\widetilde{\mathbf{H}}_{\mathbf{k}_{||}}(\mathbf{G}_1, z), \widetilde{\mathbf{H}}_{\mathbf{k}_{||}}(\mathbf{G}_2, z), \cdots\right]^{\mathsf{T}},\\ \mathbf{e}(z) &= \left[\widetilde{\mathbf{E}}_{\mathbf{k}_{||}}(\mathbf{G}_1, z), \widetilde{\mathbf{E}}_{\mathbf{k}_{||}}(\mathbf{G}_2, z), \cdots\right]^{\mathsf{T}},\\ \hat{\epsilon}_{\mathbf{G}'\mathbf{G}}(z) &= \widetilde{\epsilon}(\mathbf{G}' - \mathbf{G}, z) = \frac{1}{A_{RO}}\int_{RO} \epsilon(\mathbf{r}_{||}, z) e^{-i(\mathbf{G}'-\mathbf{G})\cdot\mathbf{r}_{||}}.\end{aligned} \tag{34}$$

In this way $\mathbf{h}$, $\mathbf{e}$ and $\hat{\epsilon}$ are the momentum representation of $\mathbf{H}$, $\mathbf{E}$ and $\epsilon(\mathbf{r}_{||}, z)$ respectively. T denotes the transpose of the row vector, and

A_{RO} represents the area where the plane wave basis is orthogonal as was discussed in Section 3.1. The Maxwell curl equations (32), written in this representation, take the form:

$$\begin{aligned}
&i\hat{k}_y h_z(z) - h_y'(z) = -i\hat{e}e_x(z),\\
&h_x'(z) - i\hat{k}_x h_z(z) = -i\hat{e}e_y(z),\\
&i\hat{k}_x h_y(z) - i\hat{k}_y h_x(z) = -i\hat{e}e_z(z),\\
&i\hat{k}_y e_z(z) - e_y'(z) = i\omega^2 h_x(z),\\
&e_x'(z) - i\hat{k}_x e_z(z) = i\omega^2 h_y(z),\\
&i\hat{k}_x e_y(z) - i\hat{k}_y e_x(z) = i\omega^2 h_z(z),
\end{aligned} \tag{35}$$

where $\hat{k}_x$ and $\hat{k}_y$ are diagonal matrices with components $(\hat{k}_x)_{GG} = k_x + G_x$ and $(\hat{k}_y)_{GG} = k_y + G_y$ respectively, and the primes denote differentiation with respect to z.

4.2 BAND STRUCTURE AND EXPANSION OF THE IN-PLANE FIELDS

The purpose here is to solve the band structure in the periodic pattern of each layer to obtain states whose z dependence are in the form of plane waves. A convenient symmetric expansion of the magnetic field, which has zero divergence, is:

$$\begin{aligned}
\mathbf{H}(\mathbf{r}_{||}, z) = \sum_{\mathbf{G}} \Bigg(&\phi_x(\mathbf{G}) \left[\hat{\mathbf{x}} - \frac{1}{q}(k_x + G_x)\hat{\mathbf{z}}\right] + \\
&\phi_y(\mathbf{G}) \left[\hat{\mathbf{y}} - \frac{1}{q}(k_y + G_y)\hat{\mathbf{z}}\right] \Bigg) e^{i(\mathbf{k}_{||}+\mathbf{G})\cdot\mathbf{r}_{||}+iqz}.
\end{aligned} \tag{36}$$

The band structure of the two-dimensional periodic pattern is used to obtain states that propagate in the direction perpendicular to the pattern.

Here $\phi_x(\mathbf{G})$ and $\phi_y(\mathbf{G})$ are the expansion coefficients, and q denotes wave number in z direction. In the momentum representation $\phi_x = [\phi_x(\mathbf{G}_1), \phi_x(\mathbf{G}_2), \cdots]^T$ and $\phi_y = [\phi_y(\mathbf{G}_1), \phi_y(\mathbf{G}_2), \cdots]^T$, therefore, the magnetic field of the expression (36) is represented as:

$$\mathbf{h}(z) = e^{iqz}\left[\phi_x\hat{\mathbf{x}} + \phi_y\hat{\mathbf{y}} - \frac{1}{q}(\hat{k}_x\phi_x + \hat{k}_y\phi_y)\hat{\mathbf{z}}\right]. \tag{37}$$

Replacing (37) in the equations (35) and multiplying by $i\hat{\eta}$, where $\hat{\eta}\hat{\epsilon} = 1$, the momentum representation for the electric field is obtained:

$$\begin{aligned}
\mathbf{e}(z) = \frac{1}{q} e^{iqz}\hat{\eta} \Big\{ &\left[\hat{k}_y\hat{k}_x\phi_x + (q^2 + \hat{k}_y\hat{k}_y)\phi_y\right]\hat{\mathbf{x}} - \\
&\left[\hat{k}_x\hat{k}_y\phi_y + (q^2 + \hat{k}_x\hat{k}_x)\phi_x\right]\hat{\mathbf{y}} + q\left[\hat{k}_y\phi_x - \hat{k}_x\phi_y\right]\hat{\mathbf{z}}\Big\}.
\end{aligned} \tag{38}$$

With the field representations $\mathbf{h}(z)$ and $\mathbf{e}(z)$, equations (35) determine two linear independent identities:

$$\begin{aligned}\omega^2\phi_x &= \left[\hat{k}_y\hat{\eta}\hat{k}_y + \hat{\eta}\left(q^2 + \hat{k}_x\hat{k}_x\right)\right]\phi_x + \left[\hat{\eta}\hat{k}_x\hat{k}_y - \hat{k}_y\hat{\eta}\hat{k}_x\right]\phi_y,\\ \omega^2\phi_y &= \left[\hat{k}_x\hat{\eta}\hat{k}_x + \hat{\eta}\left(q^2 + \hat{k}_y\hat{k}_y\right)\right]\phi_y + \left[\hat{\eta}\hat{k}_y\hat{k}_x - \hat{k}_x\hat{\eta}\hat{k}_y\right]\phi_x.\end{aligned} \tag{39}$$

The two identities (39) are reduced to the following eigenvalue problem for ω:

$$\left[\mathcal{H}(q^2 + K) + \mathcal{K}\right]\phi = \omega^2\phi, \tag{40}$$

where the blocks 2×2 K, $\mathcal{H}$, $\mathcal{K}$ and the vector ϕ are defined as:

$$\begin{aligned} K &= \begin{pmatrix}\hat{k}_x\hat{k}_x & \hat{k}_x\hat{k}_y\\ \hat{k}_y\hat{k}_x & \hat{k}_y\hat{k}_y\end{pmatrix}, & \mathcal{H} &= \begin{pmatrix}\hat{\eta} & 0\\ 0 & \hat{\eta}\end{pmatrix},\\ \mathcal{K} &= \begin{pmatrix}\hat{k}_y\hat{\eta}\hat{k}_y & -\hat{k}_y\hat{\eta}\hat{k}_x\\ -\hat{k}_x\hat{\eta}\hat{k}_y & \hat{k}_x\hat{\eta}\hat{k}_x\end{pmatrix}, & \phi &= \begin{pmatrix}\phi_x\\ \phi_y\end{pmatrix}.\end{aligned} \tag{41}$$

The band structure of the two-dimensional photonic crystal with infinite thickness (Section 3.1) can be calculated using equation (40) making $q = 0$. Reorganizing the terms in equation (40), the eigenvalue problem for q is written as:

$$\left[\mathcal{E}\left(\omega^2 - \mathcal{K}\right) - K\right]\phi = q^2\phi, \tag{42}$$

where $\mathcal{E}$ is a diagonal block matrix 2×2 of $\hat{\varepsilon}$, and satisfies $\mathcal{E}\mathcal{H} = 1$. It is important to mention that the quantities q, in the eigenvalue problem (42), can be complex even if $\mathcal{E}$ is real.

The in-plane components of the fields, in each layer of the structure, can be expanded in terms of forward and backward propagating waves with wave umbers q_n, and amplitudes a_n and b_n respectively, which are determined through the continuity conditions in each interface of the structure. In the momentum representation such expansion takes the form:

$$\begin{pmatrix}h_x(z)\\ h_y(z)\end{pmatrix} = \sum_n \begin{pmatrix}\phi_{x_n}\\ \phi_{y_n}\end{pmatrix}\left(e^{iq_nz}a_n + e^{iq_n(d-z)}b_n\right), \tag{43}$$

The forward and backward plane waves are natural solutions of the wave equation when the medium is homogeneous, which is the case of each layer in the z direction.

where d is the thickness of the layer. An arbitrary sign in q_n is chosen to make $\mathrm{Im}\{q_n\} > 0$ and prevent exponential growths in the z dependence, which would make the method unstable. The expansion (43) can be written is a more compact form:

$$h_{||}(z) = \Phi\left[\hat{f}(z)a + \hat{f}(d-z)b\right], \tag{44}$$

where Φ is a matrix with columns ϕ_n, $\hat{f}(z)$ is a diagonal matrix with components $\hat{f}(z)_{nn} = e^{iq_nz}$. $h_{||}(z)$, a and b are column vectors defined as $h_{||}(z) = [h_x(z), h_y(z)]^T$, $a = (a_1, a_2, \cdots)^T$ and $b =$

$(b_1, b_2, \cdots)^T$ respectively. In a similar way, using the expressions (37) and (38), the eigenvalue equation (40) and the magnetic field expansion (43), the equivalent electric field expansion is obtained:

$$\begin{pmatrix} -e_y(z) \\ e_x(z) \end{pmatrix} = e_{||}(z) = \left(\omega^2 - \mathcal{K}\right) \Phi \hat{q}^{-1} \left[\hat{f}(z)a - \hat{f}(d-z)b\right], \quad (45)$$

where $\hat{q}$ is a diagonal matrix with components $\hat{q}_{nn} = q_n$. The expressions for magnetic (44) and electric (45) fields can be compacted in a single matrix expression:

$$\begin{pmatrix} e_{||}(z) \\ h_{||}(z) \end{pmatrix} = M \begin{pmatrix} \hat{f}(z)a \\ \hat{f}(d-z)b \end{pmatrix}, \quad (46)$$

where M is defined as:

$$M = \begin{pmatrix} \left(\omega^2 - \mathcal{K}\right) \Phi \hat{q}^{-1} & -\left(\omega^2 - \mathcal{K}\right) \Phi \hat{q}^{-1} \\ \Phi & \Phi \end{pmatrix}. \quad (47)$$

4.3 SCATTERING MATRIX

The scattering matrix relates the amplitudes of the forward and backward propagating waves in different layers of the structure:

$$\begin{pmatrix} a_l \\ b_{l'} \end{pmatrix} = S(l', l) \begin{pmatrix} a_{l'} \\ b_l \end{pmatrix} = \begin{pmatrix} S_{11} & S_{12} \\ S_{21} & S_{22} \end{pmatrix} \begin{pmatrix} a_{l'} \\ b_l \end{pmatrix}. \quad (48)$$

The subscript l denotes the l-th layer in the multilayer media shown in Figure 8, where the forward and backward waves amplitudes are shown schematically. The fact that the scattering matrix relates the waves in different layers of the structure makes it numerically stable. It is not the case for the transfer matrix [36], in which the waves are related in the same layer, leading to numerical overflows for large $\mathbf{k} + \mathbf{G}$ [34]. The boundary conditions of $\mathbf{e}$ and $\mathbf{h}$ imply that $e_{||}$ and $h_{||}$ must be continuous in each interface of the system, *i.e.*, in $z = d$ for the layer l and $z = 0$ for the layer $l + 1$. Using the expression (46) these continuity relations become:

$$M_l \begin{pmatrix} \hat{f}_l a_l \\ b_l \end{pmatrix} = M_{l+1} \begin{pmatrix} a_{l+1} \\ \hat{f}_{l+1} b_{l+1} \end{pmatrix}. \quad (49)$$

Here $\hat{f}_l = \hat{f}_l(d_l)$. The relation (49) in terms of the matrix $I(l, l+1) = M_l^{-1} M_{l+1}$, called interface matrix, takes the form:

$$\begin{pmatrix} \hat{f}_l a_l \\ b_l \end{pmatrix} = I(l, l+1) \begin{pmatrix} a_{l+1} \\ \hat{f}_{l+1} b_{l+1} \end{pmatrix} = \begin{pmatrix} I_{11} & I_{12} \\ I_{21} & I_{22} \end{pmatrix} \begin{pmatrix} a_{l+1} \\ \hat{f}_{l+1} b_{l+1} \end{pmatrix}. \quad (50)$$

The scattering matrix $S(l', l+1)$ can be calculated recursively from $S(l', l)$ and $I(l, l+1)$ defined in (48) and (50). Eliminating the a and b dependences the block components of $S(l', l+1)$ are:

$$\begin{aligned}
S_{11}(l', l+1) &= (I_{11} - \hat{f}_l S_{12}(l', l) I_{21})^{-1} \hat{f}_l S_{11}(l', l), \\
S_{12}(l', l+1) &= (I_{11} - \hat{f}_l S_{12}(l', l) I_{21})^{-1} (\hat{f}_l S_{12}(l', l) I_{22} - I_{12}) \hat{f}_{l+1}, \\
S_{21}(l', l+1) &= S_{22}(l', l) I_{21} S_{11}(l', l+1) + S_{21}(l', l), \\
S_{22}(l', l+1) &= S_{22}(l', l) I_{21} S_{12}(l', l+1) + S_{22}(l', l) I_{22} \hat{f}_{l+1}, \quad (51)
\end{aligned}$$

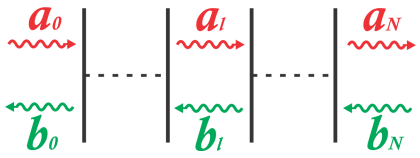

Figure 8: Multilayer system. a_i corresponds to the forward waves and b_i corresponds to the backward waves. Adapted from [34].

with the initial condition $S(l, l) = 1$. Since the matrix $\hat{f}$, which contains the evanescent behavior, is never inverted directly, the scattering matrix is stable throughout the structure. Denoting as $l = 0$ the surface of the system and $l = N$ its substrate, see Figure 8, the amplitudes a and b in each layer are defined in terms of the matrices $S(0, l)$ and $S(l, N)$:

The scattering matrix determines the causality relation between the waves entering in the system, a_0 and b_N, and the waves scattered by it, b_0 and a_N.

$$\begin{aligned}
a_l &= (1 - S_{12}(0,l) S_{21}(l,N))^{-1} (S_{11}(0,l) a_0 + S_{12}(0,l) \times \\
&\quad S_{22}(l,N) b_N), \\
b_l &= (1 - S_{21}(l,N) S_{12}(0,l))^{-1} (S_{21}(l,N) S_{11}(0,l) a_0 + \\
&\quad S_{22}(l,N) b_N). \quad (52)
\end{aligned}$$

4.4 REFLECTIVITY AND TRANSMISSION

The calculation of the reflectivity and transmission in the structure requires the vector coefficients b_0 and a_N, which represent the reflected and transmitted waves, respectively. With the scattering matrix $S(0, N)$ and the vector coefficient a_0 (the incident field), it is straightforward to obtain b_0 and a_N:

$$b_0 = S_{21}(0,N) a_0, \qquad a_N = S_{11}(0,N) a_0. \quad (53)$$

Note that a_0, b_0 and a_N are abstract representations of the incident, reflected and transmitted fields. Therefore, it is necessary to make a translation between the momentum representation and the complex

space field representation to calculate the diffractive properties. Equation (46) accomplishes this translation:

$$\begin{aligned}
\begin{pmatrix} e_{||}(0)_0 \\ h_{||}(0)_0 \end{pmatrix}_{Ref} &= M_0 \begin{pmatrix} 0 \\ \hat{f}_1(d_0)b_0 \end{pmatrix}, \\
\begin{pmatrix} e_{||}(z_t)_N \\ h_{||}(z_t)_N \end{pmatrix}_{Tra} &= M_N \begin{pmatrix} \hat{f}_1(z_t)a_N \\ 0 \end{pmatrix},
\end{aligned} \tag{54}$$

where d_0 and z_t are the perpendicular distances from the structure at which the reflectivity and transmission are calculated respectively, and the vector b_N is considered null since there is no field incident from the outside at the substrate. Taking into account that $e_{||} = [-e_y, e_x]^T$, $h_{||} = [h_x, h_y]^T$ and the z field components are obtained from the x and y components through Maxwell curl equations (35), it is possible to construct the field expansion from the expressions (33) at d_0 for reflected fields and at z_t for transmitted fields:

$$\begin{aligned}
\mathbf{H}^{Ref}(\mathbf{r}_{||}) &= \sum_{\mathbf{G}} \left(h_x^{Ref}(0)_{\mathbf{G}}\hat{\mathbf{x}} + h_y^{Ref}(0)_{\mathbf{G}}\hat{\mathbf{y}} + h_z^{Ref}(0)_{\mathbf{G}}\hat{\mathbf{z}}\right) \\
&\quad e^{i(\mathbf{k}_{||}+\mathbf{G})\cdot\mathbf{r}_{||}}, \\
\mathbf{E}^{Ref}(\mathbf{r}_{||}) &= \sum_{\mathbf{G}} \left(e_x^{Ref}(0)_{\mathbf{G}}\hat{\mathbf{x}} + e_y^{Ref}(0)_{\mathbf{G}}\hat{\mathbf{y}} + e_z^{Ref}(0)_{\mathbf{G}}\hat{\mathbf{z}}\right) \\
&\quad e^{i(\mathbf{k}_{||}+\mathbf{G})\cdot\mathbf{r}_{||}}, \\
\mathbf{H}^{Tra}(\mathbf{r}_{||}) &= \sum_{\mathbf{G}} \left(h_x^{Tra}(z_t)_{\mathbf{G}}\hat{\mathbf{x}} + h_y^{Tra}(z_t)_{\mathbf{G}}\hat{\mathbf{y}} + h_z^{Tra}(z_t)_{\mathbf{G}}\hat{\mathbf{z}}\right) \\
&\quad e^{i(\mathbf{k}_{||}+\mathbf{G})\cdot\mathbf{r}_{||}}, \\
\mathbf{E}^{Tra}(\mathbf{r}_{||}) &= \sum_{\mathbf{G}} \left(e_x^{Tra}(z_t)_{\mathbf{G}}\hat{\mathbf{x}} + e_y^{Tra}(z_t)_{\mathbf{G}}\hat{\mathbf{y}} + e_z^{Tra}(z_t)_{\mathbf{G}}\hat{\mathbf{z}}\right) \\
&\quad e^{i(\mathbf{k}_{||}+\mathbf{G})\cdot\mathbf{r}_{||}}.
\end{aligned} \tag{55}$$

Here the superscripts Ref and Tra denote the reflected and transmitted fields, respectively. To obtain the vector a_0 from the incident fields $\mathbf{H}$ and $\mathbf{E}$ their expansion coefficients, in the basis $e^{i\mathbf{G}\cdot\mathbf{r}_{||}}$, are introduced into the corresponding components of $h_{||}$ and $e_{||}$, and the translating equation (46) is used again, but now inverted:

$$a_0 = M_{0,11}^{-1} e_{||} + M_{0,12}^{-1} h_{||}. \tag{56}$$

Once the fields are expressed in the complex space, it is possible to calculate the reflectivity and transmission:

$$R = \left|\frac{\Phi_z^{Ref}}{\Phi_z^{Inc}}\right|, \qquad T = \left|\frac{\Phi_z^{Tra}}{\Phi_z^{Inc}}\right|. \tag{57}$$

Φ_z is the flux of the Poynting vector in z direction across a desired area A:

$$\Phi_z = \int_A S_z(\mathbf{r}_{||})\,da = \frac{1}{2\epsilon_0\omega c}\int_A Re\left[\mathbf{E}_{||}^*(\mathbf{r}_{||}) \times \mathbf{H}_{||}(\mathbf{r}_{||})\right] da. \tag{58}$$

The general reflectivity and transmission coefficients are calculated through the flux of the Poynting vector across a desired area.

When the integration is made in an area of orthogonality (A_{RO}) of the plane waves $e^{iG\cdot r_{||}}$, the integral (58) reduces to:

$$\Phi_z = \frac{A_{RO}}{2\epsilon_0 \omega c} Re\left[e_{||}^{\dagger} \cdot h_{||}\right]. \tag{59}$$

The operation † denotes the transposed-conjugated. Moreover, if the area of integration is a circle of radius r the integral (58) has the analytical solution[1]:

$$\Phi_z = \frac{\pi r}{\epsilon_0 \omega c} \sum_{G'G} \frac{J_1\left(r|G' - G|\right)}{|G' - G|} \left[\tilde{e}_x^*(G)\tilde{h}_y(G') - \tilde{e}_y^*(G)\tilde{h}_x(G')\right], \tag{60}$$

where J_1 is the Bessel function of order one. The equations (57) are generalized expressions to calculate R and T; when there is no pattern in the plane xy these quantities reduce to the square modulus of the well known Fresnel coefficients.

4.5 INCIDENT FIELD

With the aim of making a general description of a linearly polarized incident field, **H** and **E** can be initially written in the following form:

$$\begin{aligned} \mathbf{E} &= E_0(\cos\alpha\hat{\epsilon}_1 + \sin\alpha\hat{\epsilon}_2)e^{k_{||}\cdot\mathbf{r}_{||}}, \\ \mathbf{H} &= H_0(-\sin\alpha\hat{\epsilon}_1 + \cos\alpha\hat{\epsilon}_2)e^{k_{||}\cdot\mathbf{r}_{||}}, \\ \mathbf{k}_{||} &= k_0 \sin\theta(\cos\varphi\hat{\mathbf{x}} + \sin\varphi\hat{\mathbf{y}}), \end{aligned} \tag{61}$$

where α (polarization angle), θ (incident angle) and φ (polar angle) are defined in Figure 9, $E_0 = \epsilon_0 \omega c Z^{\frac{1}{2}}$, $H_0 = Z^{-\frac{1}{2}}$ and $k_0 = \sqrt{\epsilon}\frac{\omega}{c}$. $Z = \sqrt{\frac{\mu_0}{\epsilon_0 \epsilon}}$ is the intrinsic impedance of the external medium with dielectric constant ϵ. The polarization vectors are defined as:

$$\begin{aligned} \hat{\epsilon}_1 &= \sin\varphi\hat{\mathbf{x}} - \cos\varphi\hat{\mathbf{y}}, \\ \hat{\epsilon}_2 &= \cos\theta\cos\varphi\hat{\mathbf{x}} + \cos\theta\sin\varphi\hat{\mathbf{y}} - \sin\theta\hat{\mathbf{z}}. \end{aligned} \tag{62}$$

The TE and TM polarizations (Section 3.1) correspond to the particular cases $\alpha_{TE} = 0$ and $\alpha_{TM} = \frac{\pi}{2}$ respectively.
In many situations it is necessary to provide a specific spot shape to the incident field; this is accomplished taking advantage of the plane wave basis that describes the system: since there is a complete basis, it is possible, in principle, to expand any shape of the incident field. In practical terms the dimension of the basis must have a cutoff because only problems with finite matrices can be solved numerically in a computer; however, if the dimension is large enough, the expansion will describe this arbitrary-shape field with good accuracy. With this in mind, an arbitrary-shape function $P(\mathbf{r}_{||})$, defined to have maximum

1 The identities (73) in Appendix A are used to solve this integral.

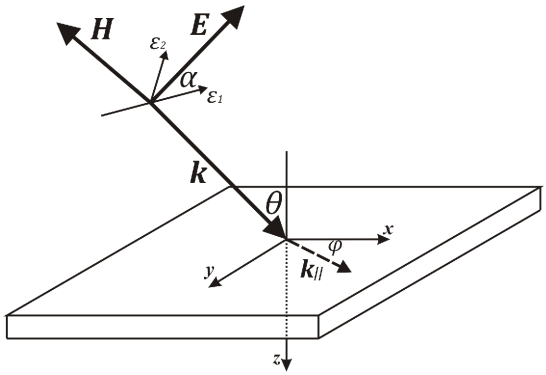

Figure 9: Scheme of the incident field in the structure. α is the polarization angle, θ is the incident angle, φ is the polar angle and the $\hat{\varepsilon}_i$ are the polarization vectors.

value 1 and minimum value 0, can be expanded with the same plane wave basis used in the patterned multilayer system:

$$P(\mathbf{r}_{||}) = \sum_{\mathbf{G}} \widetilde{P}(\mathbf{G}) e^{i\mathbf{G}\cdot\mathbf{r}_{||}}. \tag{63}$$

It is possible to take advantage of the plane wave basis to describe an arbitrary shape of the incident field.

The procedure for providing the geometrical shape of this function to the incident field is to multiply each component of such field by $P(\mathbf{r}_{||})$, consequently, the incident vector coefficients in the momentum representation become:

$$\begin{pmatrix} e_{||} \\ h_{||} \end{pmatrix}_{Inc} = \begin{pmatrix} -e_y \\ e_x \\ h_x \\ h_y \end{pmatrix} = \begin{pmatrix} -E_y \left[\widetilde{P}(\mathbf{G}_1), \widetilde{P}(\mathbf{G}_2), \cdots\right]^T \\ E_x \left[\widetilde{P}(\mathbf{G}_1), \widetilde{P}(\mathbf{G}_2), \cdots\right]^T \\ H_x \left[\widetilde{P}(\mathbf{G}_1), \widetilde{P}(\mathbf{G}_2), \cdots\right]^T \\ H_y \left[\widetilde{P}(\mathbf{G}_1), \widetilde{P}(\mathbf{G}_2), \cdots\right]^T \end{pmatrix}. \tag{64}$$

Here E_x, E_y, H_x and H_y are the field components in the expressions (61). In this way, the problem to provide a geometrical shape to the incident field is reduced to the calculation of the coefficients $\widetilde{P}(\mathbf{G})$. With the vector $\left[e_{||}, h_{||}\right]^T_{Inc}$ it is straightforward to calculate a_0 through the equation (56).

Part III

RESULTS

5

IMPLEMENTATION OF THE SCATTERING MATRIX METHOD

The scattering matrix method, as it was studied in Chapter 4, is a very powerful tool to calculate the diffractive properties of patterned multilayer structures. One special kind of these structures are photonic crystal slabs (PCS), which are two-dimensional photonic crystals with a finite thickness in the third dimension. In PCS there are two confinement mechanisms for light [37]: the distributed Bragg reflection produced by the periodic refractive index pattern, which consists in constructive and destructive electromagnetic interference phenomena throughout the crystal, and the index guiding produced by the high contrast refractive index between the slab and the external medium, which can be understood as the total internal reflection when an average refractive index for the slab is considered. PCS have become very interesting systems in the last years because their potential applications, see Chapter 1, and easier fabrication techniques at submicron length-scales. For these reasons, it is important to make a detailed study of their diffractive physical properties, which can be accomplished through the implementation of the scattering matrix method.

In this chapter it is presented how to implement the scattering matrix method in symmetric[1] PCS with L3 cavities, which are very special defects introduced in photonic crystals[2]. The particularization to L3 cavities is made with the purpose to focus in their reflectivity calculations, the principal results of this work (see Chapter 6). Nevertheless, the development exposed here is general and can be applied to another kind of defects or non-defective PCS.

5.1 IMPLEMENTATION

The scattering matrix method is implemented to calculate the reflectivity spectra of a L3 PCS cavity at normal incidence. Since there is no substrate in the photonic crystal, it can be considered as a three layer structure: a layer of thickness d interposed between two semi-infinite layers. In this way, the index l, defined in Section 4.3, takes the possible values 0, 1 and 2. Figure 10a shows a scheme of the photonic crystal in z direction. The layer $l = 1$ has a dielectric function

1 Symmetric photonic crystal slabs are characterized by having no substrate, therefore, the material below the slab is the same material above it, and consequently there is a reflection symmetry plane in the middle of the slab.

2 See Appendix B.

$\epsilon(x,y)$ which is constant along z in the layer, and contains an hexagonal photonic pattern of air holes in the plane[3]; the layers $l = 0$ and $l = 2$ have a dielectric constant associated to air, $\epsilon = 1$; and the quantities a_0, b_0 and a_2 represent the incident, reflected and transmitted waves respectively. A representative scheme of the reflectivity calculation in the L3 cavity is shown in Figure 10b. $\mathbf{E}_{Inc}$ and $\mathbf{H}_{Inc}$ refer to the incident electric and magnetic fields respectively with wave vector $\mathbf{k}_{Inc}$, φ is the polarization angle, which is the same α at normal incidence as was defined in Figure 9. The red circle with radius r_s (bigger one) in the figure corresponds to the incident excitation spot, and the green circle with radius r_a (smaller one) corresponds to the integration area of the reflected Poynting vector. Both, excitation and reflected flux calculation, are made at the same distance d_0 away from the crystal, which is incorporated in the method as the thickness of a virtual interface separating the same medium, see equation (54).

The PCS can be seen as a system of one layer with finite thickness interposed between two semi-infinite layers.

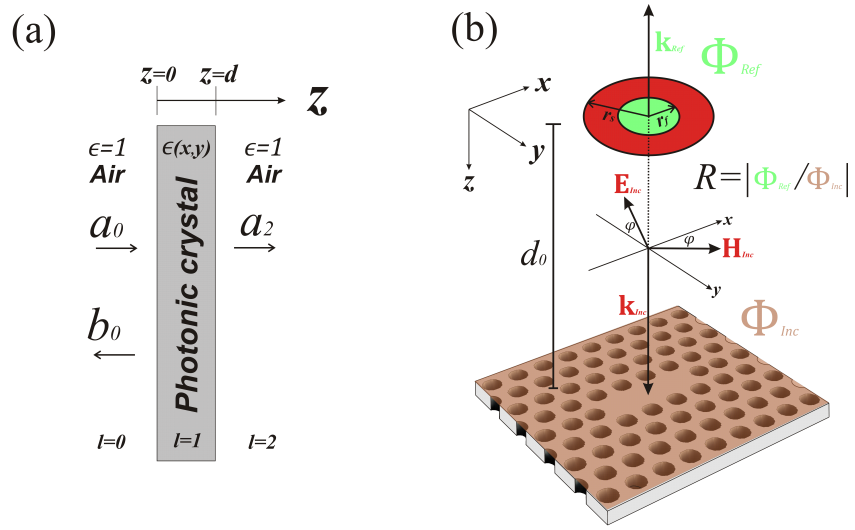

Figure 10: (a). Photonic crystal slab in the z direction: the layer $l = 0$, $l = 1$ (with thickness d) and $l = 2$ correspond to air, the photonic structure and air respectively; the incident field is represented by a_0, the reflected one by b_0, and the transmitted one by a_2. (b) Representative scheme of the reflectivity calculation: the subscripts Inc denote the incident quantities, φ is the polarization angle; r_s and r_a denote the radius of the incident spot and the radius of the Poyting flux area respectively; d_0 is the distance at which the crystal is excited and at which the reflectivity is calculated.

5.2 CROSS-POLARIZED REFLECTIVITY CALCULATIONS

Currently, it has become usual to measure reflectivity spectra of photonic crystals by cross-polarized spectroscopy [38], which consists in

3 See Appendix A.

collecting the reflected radiation from the sample at orthogonal polarization with respect to the incident radiation. This filters the incident light and ensures a measurement of the sample response only. It is possible to implement a cross-polarized calculation in the scattering matrix formalism projecting the in-plane reflected fields in a new system $x'y'$ rotated counterclockwise by an angle φ (the same angle of polarization), and remaining only with the cross-polarized contribution of the Poynting vector to calculate the reflected flux. Figure 11 shows the cross-polarized scheme; in the coordinate system xy the z component of the Poynting vector is $S_z^{Ref} = \left(E_x^* H_y - E_y^* H_x\right)^{Ref}$, on the other hand, in the coordinate system $x'y'$ the z component of the Poynting vector, which is the same as in the system xy, can be written as $S_z^{Ref} = \left(S_z^{Cross} - E_{y'}^*, H_{x'}\right)^{Ref}$, where $S_z^{Cross,Ref} = \left(E_{x'}^*, H_{y'}\right)^{Ref}$. Therefore, a cross-polarized calculation is accomplished if there is considered only the contribution $S_z^{Cross,Ref}$ in the flux integral (58). The xy components are related to the $x'y'$ ones through a basic coordinate transformation:

The cross-polarized spectroscopy minimizes the background noise and allows a measurement of the sample response only.

$$\begin{pmatrix} V_{x'} \\ V_{y'} \end{pmatrix} = \begin{pmatrix} \cos\varphi & \sin\varphi \\ -\sin\varphi & \cos\varphi \end{pmatrix} \begin{pmatrix} V_x \\ V_y \end{pmatrix}. \tag{65}$$

The vector $\mathbf{V}$ represents the transformations of both the magnetic and electric fields. In this way, it is straightforward to show that in terms of the reflected fields in the system xy, $S_z^{Cross,Ref}$ takes the form:

$$\begin{aligned} S_z^{Cross,Ref} = &\left(\cos^2\varphi E_x^* H_y - \sin^2\varphi E_y^* H_x + \right. \\ &\left. \cos\varphi \sin\varphi \left(E_y^* H_y - E_x^* H_x\right)\right)^{Ref}. \end{aligned} \tag{66}$$

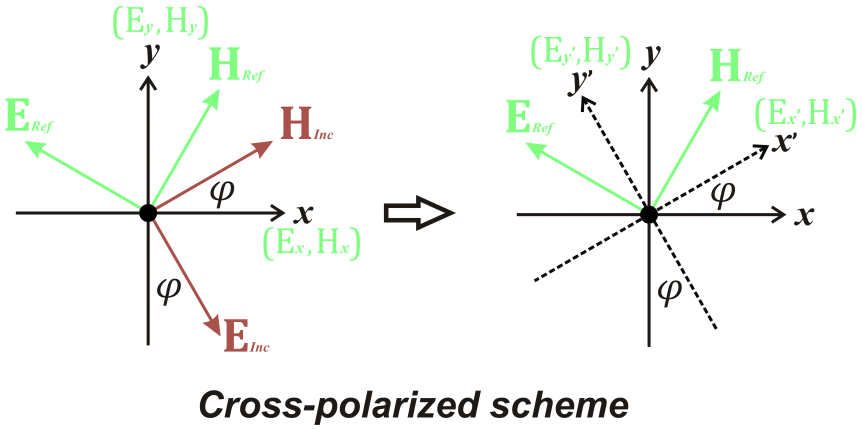

Figure 11: Cross-polarized implementation. The system is rotated counterclockwise by an angle which is the same angle of the incident field polarization; the reflected fields are projected in this new system.

6

REFLECTIVITY CALCULATIONS IN L3 PHOTONIC CRYSTAL SLAB CAVITIES

In photonic crystal slabs the incoming excitation induces interference between the electromagnetic modes quasi-confined throughout the plane of the structure (guided resonances) and the radiative field outside [39], therefore, the reflectivity spectrum is characterized to have asymmetrical sharp peaks which can be recognized as Fano resonances [40]. The asymmetry factor q in the Fano resonance, which is a quantifier of the asymmetry degree of the lineshape, may be controlled by the angle of incidence of the excitation field, which controls the phase between the continuum and the discrete channel [41, 42, 43], and/or the geometrical parameters which control the effective coupling parameter between the two channels [44, 45]. When an optical cavity is generated in the photonic crystal slab by the introduction of a defect in the periodic pattern, the Fano resonance phenomenon is produced by the interference of the radiation reflected by the cavity (scattering by a discrete state) and the light reflected by the crystal pattern (scattering to the continuum) [46]. Here, the asymmetry factor may be controlled, for instance, through the size of the excitation spot [47], which can be understood as a way to increase or decrease the contribution of the scattering to the continuum.

In the present work the polarization of the incoming light is used as a new way to accurately control the interference between a discrete state, the fundamental mode of the L3 photonic crystal cavity, and a continuum of electromagnetic states, the radiation scattered by the photonic crystal pattern. The reflectivity of the crystal is modeled using the scattering matrix (SM) formalism presented in Chapter 4 and implemented in Chapter 5. Good agreement is obtained with experimental results.

6.1 THEORETICAL RESULTS

Using frequency domain simulations it is found that the photonic crystal slab of hexagonal lattice of holes has a full TE-like band gap when the refractive index is $n = 3.5$, with hole radius $r = 0.29$ and slab thickness $d = 0.5a$. In this way, confined modes can be supported by point defects as L3 cavities. Once such cavity is introduced in the crystal, Finite difference time domain (FDTD) simulations show that the frequency ν of the fundamental mode at $s = 0.15a$ [1] is 0.26926 c/a,

1 See Appendix B.

which corresponds to 1.28505 eV [2] or a vacuum wavelength of 965.609 nm when the lattice parameter is $a = 260$ nm. The purpose to make these preliminary simulations, presented in Appendix B, is to determine the energy window where it will be expected to find the mode resonance in the SM calculations. Figure 12 shows the convergence of the fundamental mode energy for the SM method as a function of the number of plane waves used to expand the field. The intensity distribution is shown for each point in the graphic, which becomes better defined when the number of plane waves increases. The supercell was chosen to have an area of $12a \times 12a\sqrt{3}$. From the figure, it can be seen also that the convergence in the energy is achieved for a number of plane waves higher than approximately 750. However, for such a large number of waves, the contribution from other supercells to the reflectivity spectrum becomes significant. The size of the supercell could be increased to prevent this but the computational cost would increase enormously. Since the interest in this work is the reflectivity spectrum and not so much in the exact mode energy, the calculations that will be presented in the remainder of the chapter were made using 441 plane waves, which determine a well defined field distribution and a low contribution of the others supercells to characterize the reflectivity of only one cavity.

441 plane waves determine a well defined field distribution and a low contribution of the others supercells.

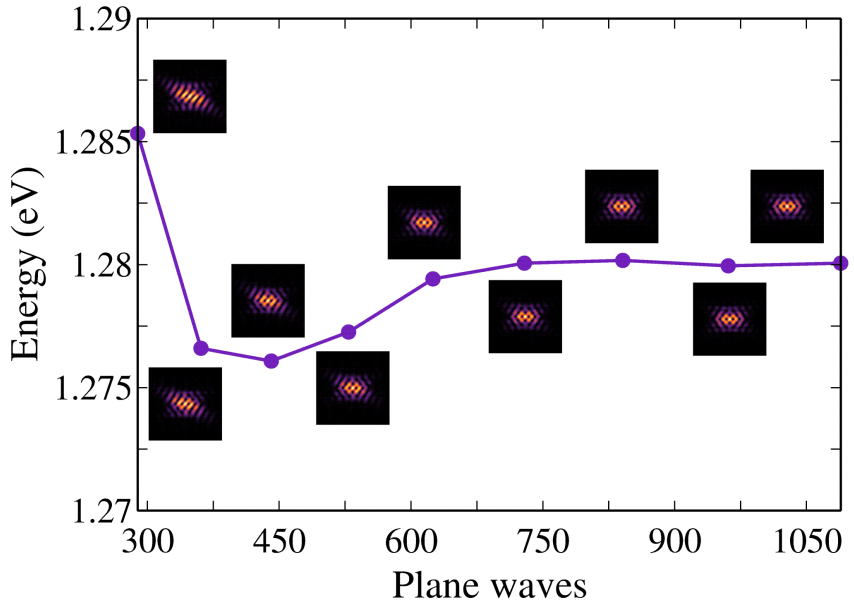

Figure 12: Convergence of the fundamental mode energy in the SM method as function of the plane wave basis dimension. The intensity distribution of the mode is shown also for each point in the graphic.

It is important to take into account that the number of plane waves reported in Figure 12 corresponds to the expansion of each in-plane

2 The energy $\hbar\omega$ of one photon of frequency ω.

field components only, making the dimensionality of the complete problem much larger. If N is the number of plane waves, the eigenvalue problem (42) has dimensionality $2N \times 2N$, and the matrices M (47), S (48) and I (50) have dimensionality of $4N \times 4N$.

Figure 13 shows the adopted system to make the reflectivity calculations. The dielectric function (left) defines a supercell with superlattice parameter $A = 12a$ and area $12a \times 12a\sqrt{3}$ (the same used in the convergence analysis of Figure 12), which ensures a cavity isolated enough to prevent significant field overlapping between neighbors cavities; the intensity distribution of the fundamental mode (right) evidences this low overlapping.

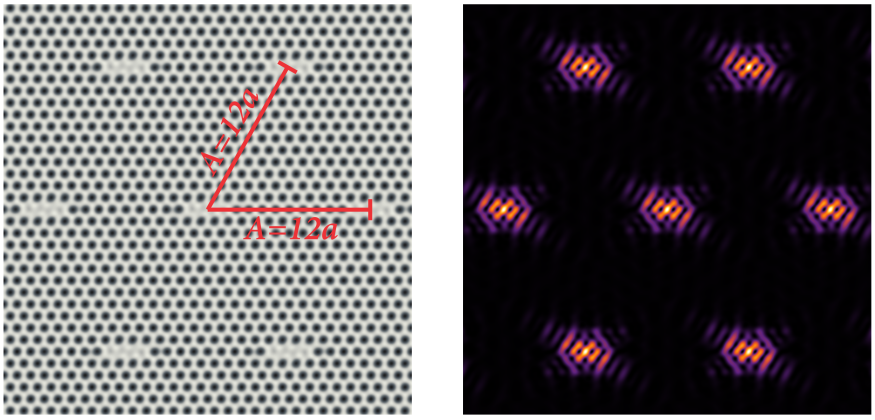

Figure 13: (Left) Dielectric function of the supercell adopted with superlattice parameter $A = 12a$. (Right) Intensity distribution of the fundamental L3 cavity mode.

To calculate the reflectivity spectrum the incident field is chosen to have a circular shape of radius $r_s = 2.15a$ with the purpose to excite only the cavity. The $\widetilde{P}(\mathbf{G})$ coefficients (63) of this geometrical shape are easily computed using the identities (73). The vertical distance at which the crystal is excited and at which the Poynting vector flux is calculated is fixed at $d_0 = 20a$, representing a middle distance between the near and far field regimes. In addition to this, since there are many supercells as plane waves in the basis, the radius r_f of the flux area must be appropriately chosen to collect radiation of only one supercell. In the reflection process of the crystal it is expected a Fano resonance which is product of the electromagnetic interference between the radiation reflected by the cavity and the radiation reflected by the crystal pattern; if the discrete and continuum contributions to the interference are comparable the resonance peak is characterized to have a sharp asymmetrical shape, moreover, if the continuum contribution is dominant the resonance becomes a Lorentzian symmetrical peak [46]. With this in mind, a symmetrical peak is expected if the cavity mode contribution to the reflection process is low, which cor-

The L3 cavity is excited with a circular spot at a distance of 20a from the crystal, with the purpose to simulate usual experimental conditions.

responds to the cases $\varphi = 0°$ (the incident field polarization matches the dominant mode polarization) and $\varphi = 90°$ (the orthogonal direction to the dominant mode polarization) in a cross-polarized scheme[3].

When only one supercell contributes to the Fano interference, it is expected symmetrical lineshapes at 0° and 90° in the cross-polarized reflectivity spectrum.

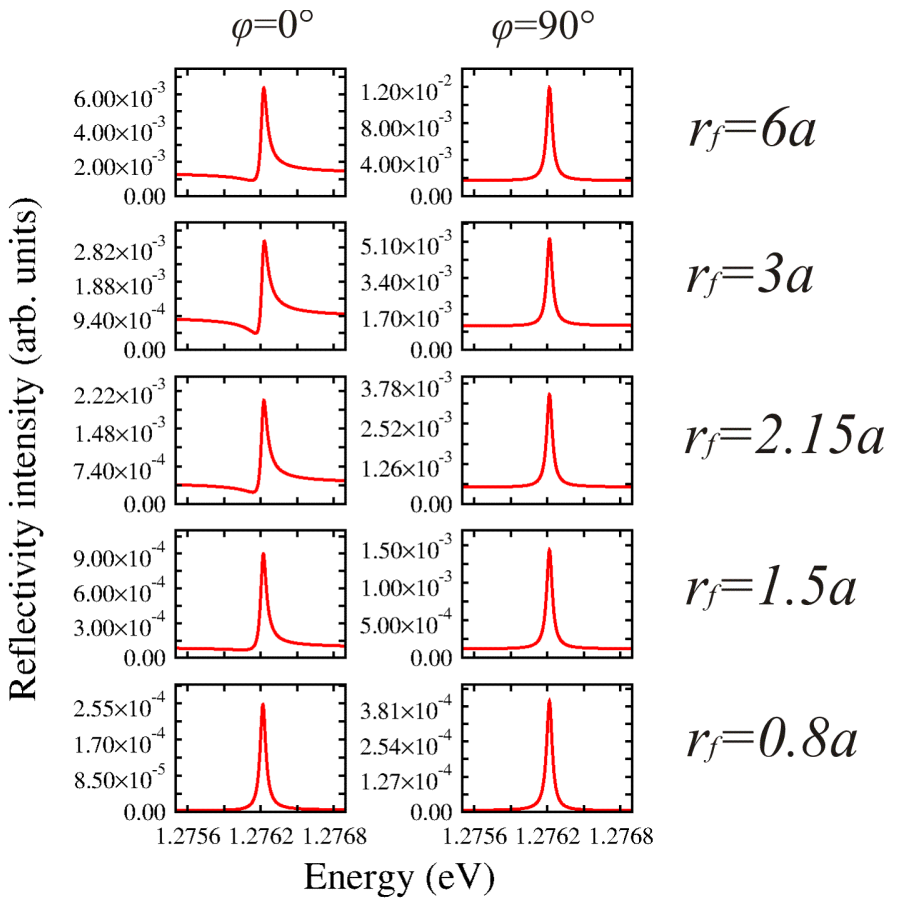

Figure 14: Cross-polarized reflectivity spectrum for the cases $\varphi = 0°$ and $\varphi = 90°$ at different collection radius r_f. The appropriated value of r_f, at which the lineshapes becomes symmetrical, is found to be $0.8a$.

When the mode is efficiently excited at 0°, the collection is performed in a direction at which the emission of the cavity is low with respect to the continuum contribution. Similarly, when the mode is not efficiently excited at 90°, the continuum is also dominant due to the orthogonal collection. In the theoretical model, collection is understood as the integration of the Poynting vector (58). With these physical ideas, whose origin comes from the Fano interference phenomenon, it is possible to find the appropriated r_f to collect radiation of only one supercell: r_f is reduced until symmetrical peaks at 0° and 90° in the reflectivity spectrum are obtained. Figure 14 shows the results obtained. The asymmetrical shapes at radius larger than $0.8a$ come from

3 See Figure 10, Figure 11 and Appendix B.

the interference with another supercells, in this way, 0.8a is an appropriated value for r_f to make the polarization-dependent reflectivity calculations.
It is important to take into account that the appropriated value of r_f depends of the perpendicular distance d_0, therefore, if such distance is changed the analysis of Figure 14 must be made again. If a cross-polarized scheme is not considered when $r_f = 0.8a$, Fano interference takes place for the 0° and 90° angles, meaning that the discrete and continuum contributions are comparable. Figure 15 evidences this fact, showing the reflectivity spectrum for these cases without cross-polarized calculations.

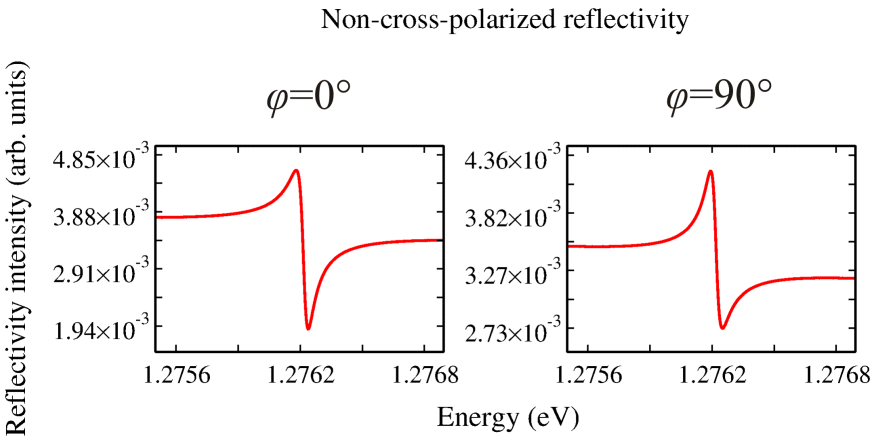

Figure 15: Non-cross-polarized reflectivity spectrum for the cases 0° and 90° when $r_f = 0.8a$. The discrete and continuum contributions are comparable and a Fano interference takes place.

The polarization-dependent reflectivity spectrum is shown in Figure 16 for several values of φ. At $\varphi = 0°$, as it was discussed above, it is expected a symmetrical lineshape. The degree of asymmetry increases with the polarization angle, until the lineshape is symmetric but inverted at 52.7°, meaning a Lorentzian transmission of the mode. Above this angle the lines become asymmetrical again, albeit with reversed shape. Finally, the degree of asymmetry decreases, reaching the symmetric case again at $\varphi = 90°$. Figure 16 evidences that the degree of asymmetry can be controlled through the polarization angle of the incident wave, being possible to reverse the lineshape of the Fano resonance. This phenomenon was already reported by Driessen *et al* [42] and Babic *et al* [43] with the difference that they used the angle of incidence to control the lineshape of the resonance. In this way, the polarization angle of the incident field is another important parameter which can be explored to tune the Fano interference process.

The degree of asymmetry in the Fano resonance can be controlled through the polarization angle of the incident field.

The electromagnetic interference producing the characteristic sharp peaks in Figure 16 depends on the relative contribution of the scattering through the L3 fundamental mode and the scattering by the photonic crystal pattern. This can be controlled through the polarization of the incident radiation, which controls the effective phase difference between the two scattering channels.

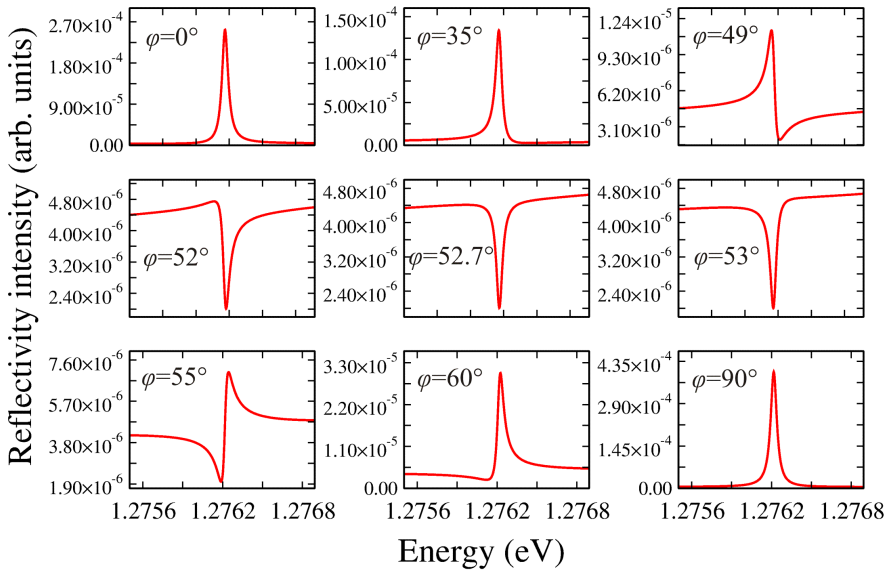

Figure 16: Cross-polarized polarization-dependent reflectivity spectrum for the polarization angles 0°, 35°, 49°, 52°, 52.7°, 53°, 55°, 60° and 90°. The Fano lineshape is controlled and reversed by the polarization angle.

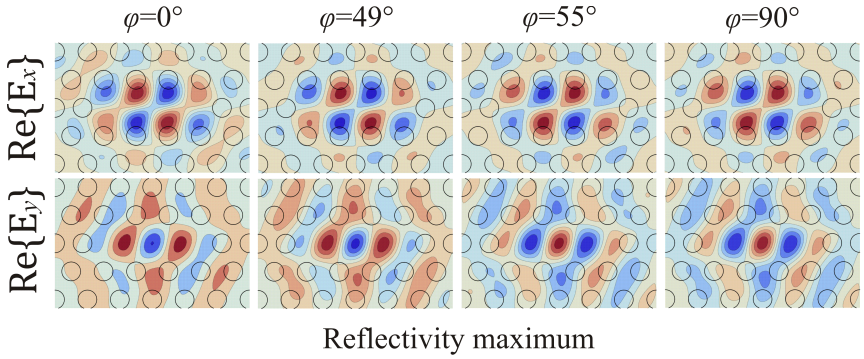

Figure 17: Field distribution in the middle of the crystal at the reflectivity maxima of Figure 16 for the cases $\varphi = 0°, 49°, 55°$ and 90°. There is a change of the mode phase when the Fano lineshape is reversed.

Figure 17 shows the real part of the E_x and E_y components for the cases $\varphi = 0°, 49°, 55°$ and 90° at the reflectivity maxima of Figure 16.

Considering that blue and red correspond to the minimum and maximum values respectively in the contourplot, there is a clear phase change of the mode in function of the polarization angle of the incident field. The cases $\varphi = 49°$ and $\varphi = 55°$, which have associated reversed lineshapes in Figure 16, evidence opposite phases in their field distributions. Such phase change remains until the symmetric lineshape at 90° is attained, generating an opposite phase between the symmetrical cases at 0° and 90°.

The incident field polarization affects the relative phase between the discrete and continuum contribution, and consequently the lineshape of the Fano resonance.

Since not only the mode field contributes to the Fano interference, it is important to examine the field outside the crystal, which contains the continuum contribution. Figure 18 show the field distributions $\mathrm{Re}\{E_x\}$, $\mathrm{Re}\{E_y\}$ and $\mathrm{Re}\{E_z\}$ in the transversal planes $x = 0$ and $y = 0$ for the same 49° and 55° cases. The excitation field is incident from bottom to top. Outside the crystal there is not a significative phase change of the field, the relative maxima and minima remain stable as the polarization angle is changed, producing the reversal of the lineshape. In this way, the polarization angle of the incident wave changes significantly only the phase of the mode, and consequently the relative phase between the discrete and continuum contribution.

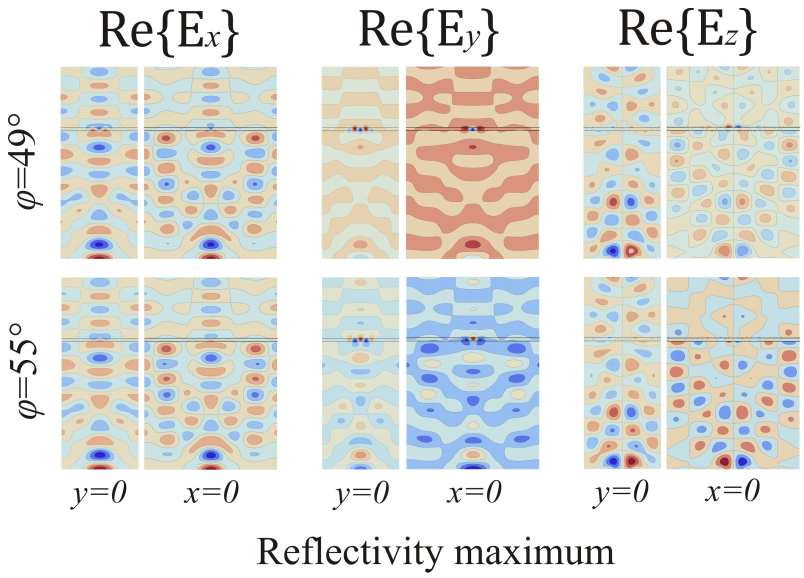

Figure 18: Field distribution in the planes $x = 0$ and $y = 0$ for the cases $\varphi = 49°$ and $\varphi = 55°$. The crystal is indicated with black lines. The phase of the continuum does not change significantly.

As it was already mentioned above, the Fano resonance takes place in systems where it is possible to observe interference between a discrete channel and a continuum background. The most intuitive explanation of its physical meaning is given by the analysis of a classical analog: two weakly coupled driven-damped classical oscillators, as depicted in Figure 19. At a frequency close to the second normal mode of the coupled system, in which the two oscillators move in opposite direc-

tions at frequency $\omega+$ it is possible to achieve a zero value of the amplitude C_1 of oscillator 1, since there are two effective driving forces, out of phase, acting on this oscillator and the net effect is to cancel its motion. Out of this special anti-resonant condition (resonant destructive interference), oscillator 1 recovers a non-zero amplitude. As a result, the amplitude function C_1 presents a sharp asymmetrical peak centered close to $\omega+$, which is roughly the resonant frequency ω_2 of the second oscillator, for a weak coupling condition [48]. In this view, the harmonically oscillating driving force may be considered as the continuum channel, while the discrete channel is the oscillator mode. The degree of asymmetry of the Fano resonance, which is quantified by the asymmetry factor q, is determined by the coupling parameter and the phase between the driving force and the oscillator mode [4].

The characteristic asymmetrical peak in the Fano resonance can be understood as phenomena of resonant destructive and resonant constructive interferences.

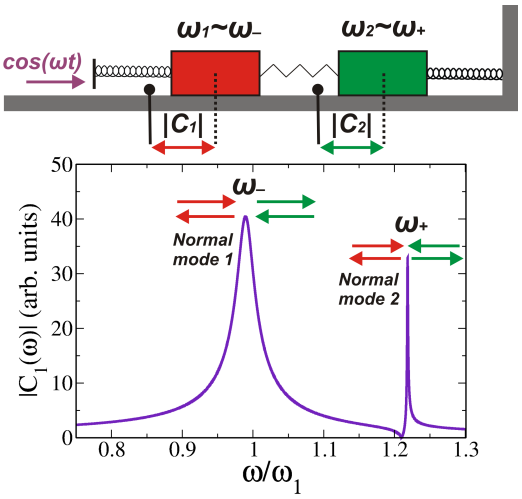

Figure 19: Two coupled classical damped oscillators driven by an harmonic force $\cos(\omega t)$. At weak coupling $\omega_1 \backsimeq \omega_-$ and $\omega_2 = 1.2\omega_1 \backsimeq \omega_+$, where ω_1 and ω_2 are the resonant frequencies of the oscillators and ω_- and ω_+ are the resonant frequencies of the normal modes. Oscillator 1 shows an anti-resonance phenomenon which generates an asymmetric lineshape of its amplitude function C_1 when the system is oscillating at frequencies around the second normal mode (ω_+). Adapted from reference [48].

With this classical analog in mind, it is possible to understand the Fano phenomenon in the photonic crystal as a simple electromagnetic interference between the two scattering channels: a discrete and a continuum. When a reflectivity maximum occurs the two channels interfere constructively in the reflection region, and when a reflectivity minimum occurs they interfere destructively. In this way, it is

4 When the continuum contribution is dominant the magnitude $|q|$ tends to infinity and determines a symmetrical lineshape, or Lorentzian shape. When the continuum contribution is comparable to the discrete one the magnitude $|q|$ is close to 1 and determines an asymmetrical lineshape. Finally, when $q = 0$ the lineshape is symmetrical but inverted.

expected a phase difference between the fields at the reflectivity minimum and at the reflectivity maximum in the Fano lineshape. Figure 20 shows this fact: there the real and imaginary part of the in-plane electric field components for the polarization angles $\varphi = 49°$ and $\varphi = 55°$ is plotted at the reflectivity minimum and maximum. The case $\varphi = 49°$ exhibits a clear change of phase between the minimum and maximum in its real part for both fields components. The imaginary part undergoes no significant changes; the real part carries the information of the phase change. Moreover, the case $\varphi = 55°$ exhibits also the change of phase but now in its imaginary part, due to the additional phase introduced by the polarized incident field, as it was shown in Figure 17. Here the imaginary part carries the information of the phase change in the Fano resonance.

The asymmetrical peak in the reflectivity spectrum corresponds to destructive, at the minimum, and constructive, at the maximum, electromagnetic interference phenomena in the reflection region.

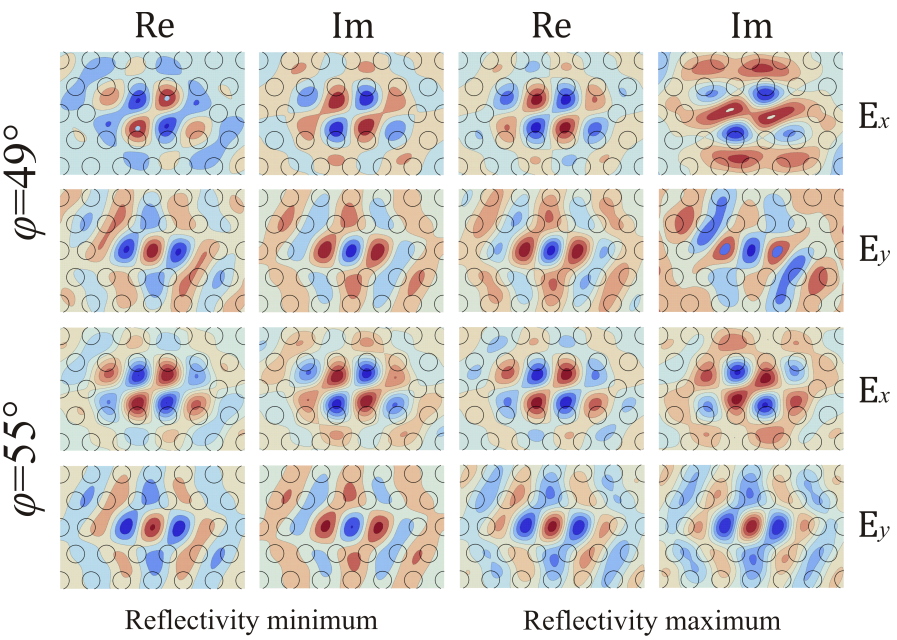

Figure 20: Real and imaginary parts of the in-plane electric field components for the cases $\varphi = 49°$ and $\varphi = 55°$ at the reflectivity minimum and maximum. For $\varphi = 49°$ and $\varphi = 55°$ the information of the phase change is carried by the real and imaginary parts respectively.

Another interesting effect that can be studied with the SM method is the enhancement of the continuum contribution through increasing the radius of the excitation spot. When the continuum contribution is dominant the lineshape of the Fano resonance becomes symmetrical. This phenomenon, first reported in the experimental work performed by Galli *et al* [47], is fully reproduced by the SM method. The results are shown in Figure 21 for the polarization angles $\varphi = 55°$ and $\varphi = 60°$. The lineshapes become symmetrical when the spot radius r_s

increases until its maximum value $r_s = 6a$ [5]. The other polarization angles determine also symmetrical lineshapes when $r_s = 6a$, producing $|q|$ values larger than 39 after fitting the spectrum with the Fano formula (see below).

The continuum contribution can be enhanced increasing the size of the excitation spot.

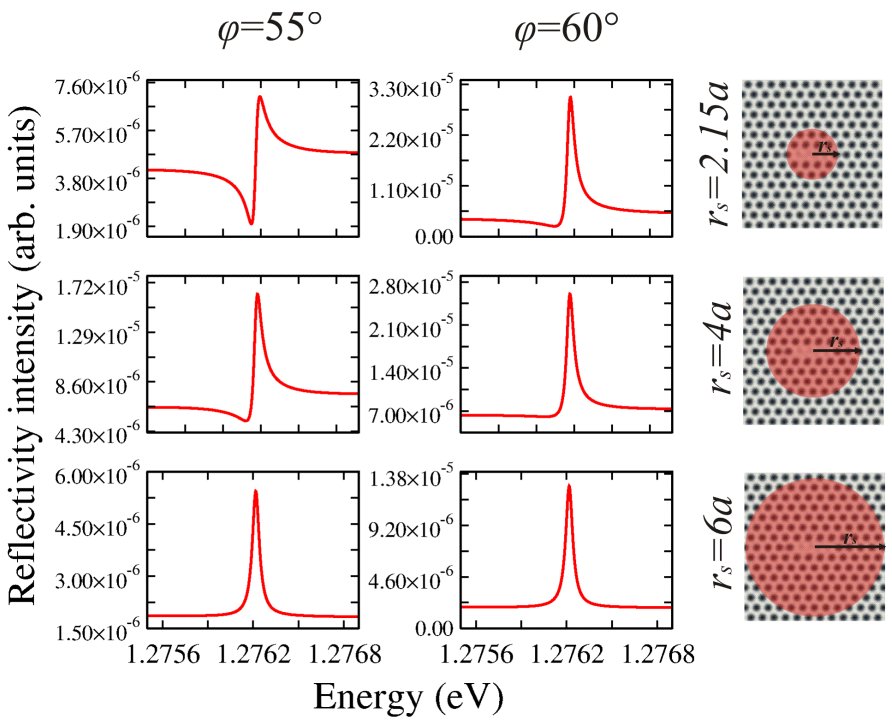

Figure 21: Cross-polarized reflectivity spectrum for the cases $\varphi = 55°$ and $\varphi = 60°$ at different excitation spot radius r_s. The lineshapes become symmetrical when r_s is high with respect to the cavity size.

6.2 EXPERIMENTAL RESULTS

Polarization resolved reflectivity experiments were made by Pablo T. Valentim and collaborators [49] to study the Fano interference phenomenon on GaAs slab photonic crystal L3 cavities. The sample was fabricated from a GaAs wafer by electron beam lithography and reactive ion etching. Free standing GaAs membranes of 130 nm thickness, patterned with a hexagonal lattice of circular air holes, were fabricated with lattice parameters in the range $230 \leqslant a \leqslant 260$ nm and fill factors $0.25 \leqslant r/a \leqslant 0.33$. The membranes were obtained by selective etching of a 1 µm thick $Al_{0.6}Ga_{0.4}As$ sacrificial layer. The L3 cavity consists of a line of three missing holes at the center of the structure with its two end holes displaced outwards by $0.15a$ to increase the quality factor. The L3 cavity fundamental mode is around 940–1020

5 A higher value of r_s would overlap with the neighboring supercells, which produces undesired effects in this calculation.

nm and its quality factor is roughly 7000.

The experimental setup for the polarization resolved reflectivity measurements is shown in Figure 22. The sample is excited with white light. A 970 nm band pass filter (BPF) in the path of the white light restricts the range of wavelengths to an interval of 960 nm to 980 nm. To decrease the background, the reflectivity is measured by cross-polarized spectroscopy [38]. For this, a polarizing beam splitter (PBS) is placed before the objective lens, allowing to excite and collect signal from the sample in orthogonal polarizations, $|V\rangle$ and $|H\rangle$. The polarization angle φ of the excitation light is adjusted by a half-wave plate (HWP) placed between the PBS and the objective lens. As shown in the figure, this angle is defined relative to the direction orthogonal to the L3 cavity, i.e., perpendicular to the line of missing holes. A confocal arrangement of two 20 mm lenses and a 100 µm diameter pinhole placed in the collection path allows us to collect light exclusively from a small area around the cavity.

The reflectivity is measured by cross-polarized spectroscopy on GaAs slab photonic crystal L3 cavities.

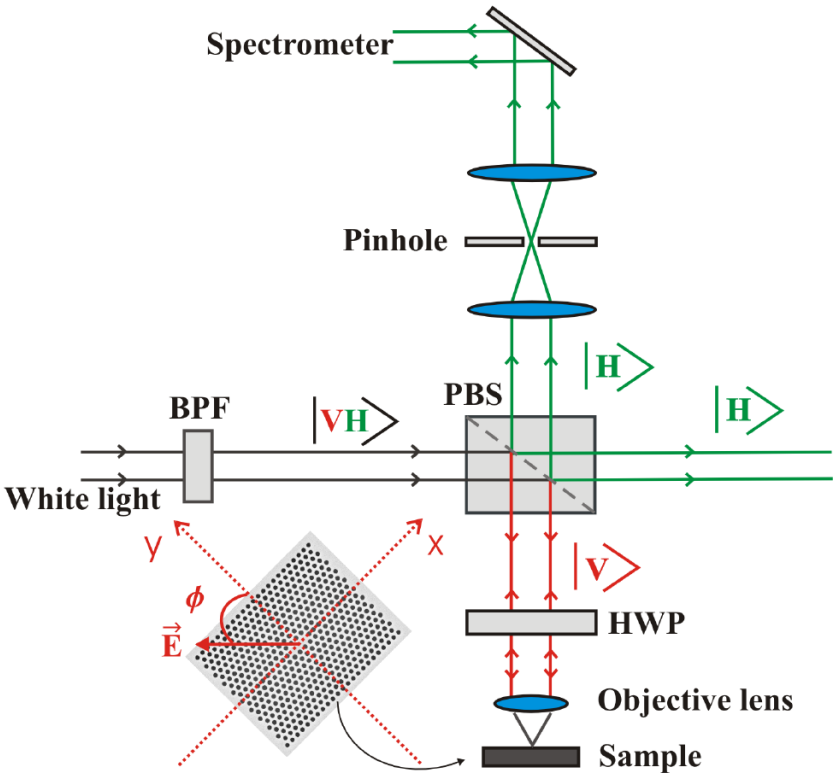

Figure 22: Experimental setup for the polarization resolved reflectivity measurements, as described in the text. The lower left inset is a scanning electron microscopy (SEM) image of one of the samples, showing the definition of the polarization angle.

Figure 23 shows a set of reflectivity spectra, each obtained for different linear polarizations of the incoming white light. To determine the

polarization angle φ relative to the photonic crystal cavity axes, the photoluminescence emission of the fundamental mode is used as a guide. A symmetrical reflectivity lineshape is seen at $\varphi = 0°$, as it is expected if a Fano interference phenomenon is occurring (see discussion above). When the HWP is rotated, increasing the polarization angle, the reflectivity line changes from a symmetrical to an asymmetrical shape, suggesting that the discrete L3 cavity mode and the background of continuum states are indeed interfering in the way predicted by Fano [40].

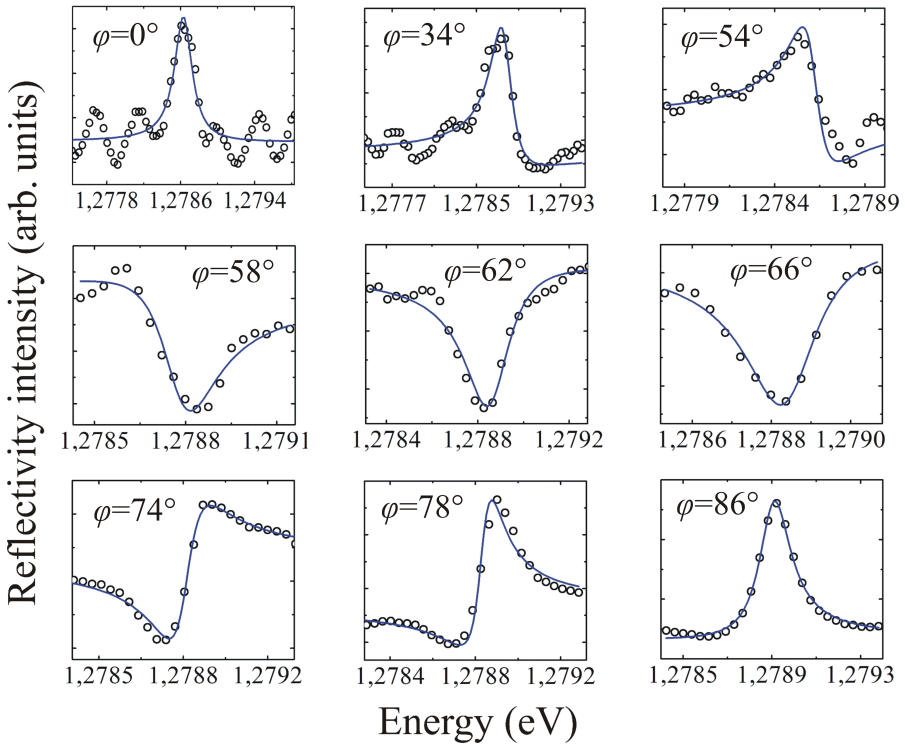

Figure 23: Representative reflectivity spectra for nine polarization angles of the exciting light. The dots are the experimental data and the curves are fits obtained with the Fano formula (67) as discussed in the text. The fit parameter q for each polarization angle is indicated.

The experimental reflectivity is well fitted by the Fano interference formula as expected from the theory.

In a first simple approach, the reflectivity spectra are fitted using the Fano formula:

$$R = R_0 + A\frac{\left(\frac{2(E-E_0)}{\Gamma} + q\right)^2}{\left(\frac{2(E-E_0)}{\Gamma}\right)^2 + 1}, \tag{67}$$

where R, R_0, A, q, Γ, E and E_0 respectively stand for the peak intensity, background off-set, the amplitude constant, the Fano asymmetry factor, line width, energy and resonance energy. The fits obtained with

this formula are shown by the solid curves in Figure 23. The asymmetry factors q given by the fits are stated for each polarization.
Figure 24 shows the asymmetry factor q as function of the polarization angle for the experimental (left) and theoretical (right) cases fitted with equation (67). As expected from the good qualitative agreement between the theoretical and experimental lineshapes shown in Figure 16 and Figure 23 respectively, the agreement here is also qualitatively good, meaning that the overall dependence of the Fano interference phenomenon on the polarization is well described.

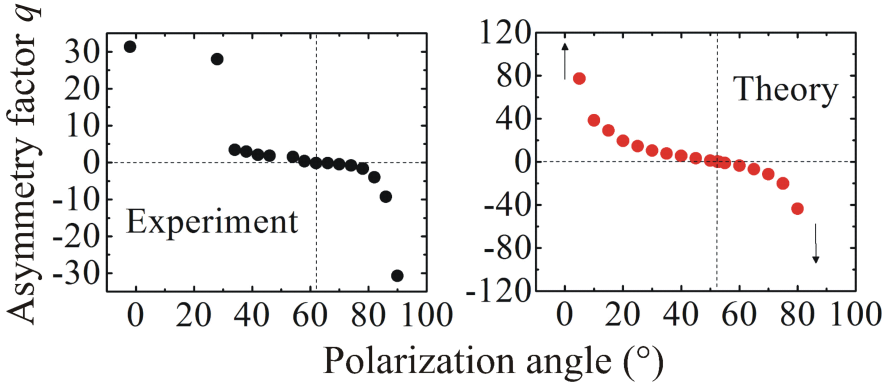

Figure 24: Asymmetry factor as a function of the polarization angle for experimental results (left) and theoretical calculations (right).

The spot size dependent experiments were made using the same setup presented in Figure 22, the size is controlled changing the laser focus incident on the sample. The results are shown in Figure 25 for the spot diameters $D_s \sim 2\mu m$ and $D_s \sim 10\mu m$. These results are in good agreement with the theoretical ones shown in Figure 21.

The behavior of the asymmetry q factor and the spot-size dependent lineshape are qualitatively in good agreement with the theoretical calculations.

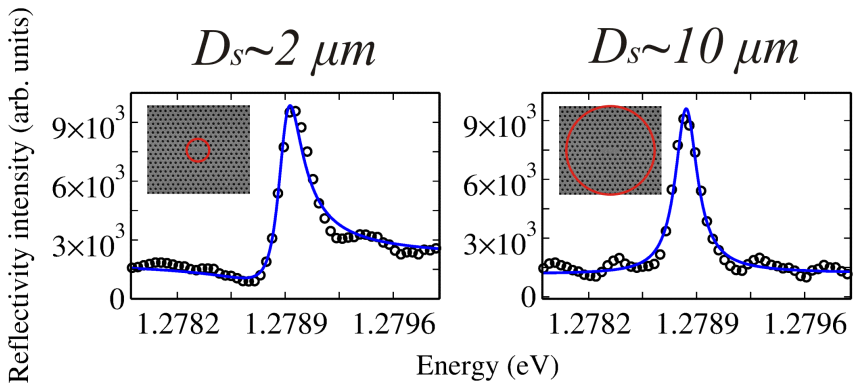

Figure 25: Reflectivity spectrum when the laser is focused on the cavity with spot diameter $D_s \sim 2\mu m$, and defocused, with $D_s \sim 10\mu m$.

7

CONCLUSIONS AND PERSPECTIVES

In the development of this work, the plane wave expansion and the scattering matrix method were presented as two powerful tools to investigate the electromagnetic properties of photonic crystals. The hybrid method, introduced initially by Whittaker *et al.* [34] and with the strategic modifications to describe arbitrary geometrical excitation spots, showed its great generality to characterize processes in photonic crystals involving scattering states, which is a requirement to study an universal phenomenon such as Fano resonances. The results of this work give a clear insight about the Fano interference process in the L3 photonic crystal slab cavity. First of all, the polarization of the excitation field incident on the crystal is an important parameter to take into account in the reflectivity calculations of this kind of cavities, whose modes have a well defined polarization. And second, the interference phenomenon depends on the relative contribution of the scattering through the discrete state and the scattering to the continuum. Since in the photonic crystal this phenomenon is produced by the electromagnetic interference between these two channels, the relative contribution can be controlled through the effective phase difference between them. Therefore, the polarization of the incident radiation can be used to control the effective phase difference between the scattering through the L3 fundamental mode and the scattering through the photonic crystal pattern. The scattering matrix implementation here allowed to reproduce the experimental results reported by Galli *et al.* [47], in which the spot size can be used to enhance the continuum contribution in the electromagnetic Fano interference.

The implemented method can be used to study the diffractive properties in a great variety of complex photonic structures, nevertheless, it is important to take into account the introduced approximations, as the supercell environment, finiteness of the basis and distance at which the reflectivity is calculated (near and far field regimes). The next step in this work is to find efficient ways to overcome these limitations and obtain a better agreement between the experimental and theoretical results.

Part IV

APPENDIX

A

FOURIER COEFFICIENTS OF $\epsilon(x, y)$

Most of the work invested in the calculation of band diagrams for photonic crystals is focused on finding the expansion coefficients of $\epsilon(x, y)$ in the plane wave basis that describes the crystal. In this appendix it is shown how to calculate these coefficients in the square and hexagonal lattices of cylinders (or holes) for defective and non-defective photonic crystals.

A.1 SQUARE LATTICE

The reciprocal lattice vector of the square lattice is:

$$\mathbf{G} = \frac{2\pi j}{a}\hat{\mathbf{x}} + \frac{2\pi m}{a}\hat{\mathbf{y}}, \tag{68}$$

where j and m are integer numbers. The expansion of the dielectric function in terms of a plane wave basis with the periodicity of the Bravais lattice can be written as:

$$\epsilon(x, y) = \sum_{j\,m} \epsilon_{j\,m}\, e^{i\frac{2\pi}{a}(xj+ym)}. \tag{69}$$

To find the $\epsilon_{j\,m}$ coefficients of the expression (69), the function $\epsilon(x, y)$ is multiplied by $e^{-i\frac{2\pi}{a}(xj'+ym')}$ (another element of the basis) and integrated in the orthogonality region of the basis, which in this case, is the unit cell of the crystal (UC). Figure 26 schematizes this region.

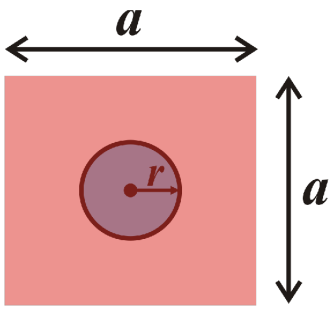

Figure 26: Integration region of the square lattice.

The integration produces two Kronecker delta functions which make zero all the terms different from the cases $m = m'$ and $n = n'$. In this way, $\epsilon_{j\,m}$ takes the form:

$$\epsilon_{j\,m} = \frac{1}{a^2}\int_{UC} \epsilon(x, y)\, e^{-i\frac{2\pi}{a}(xj+ym)}\, da. \tag{70}$$

The integral (70) can be divided in two contributions: one corresponding to the square region, and the other one corresponding to the circular region. If ϵ_r is the dielectric constant of the cylinders and ϵ_s is the dielectric constant of the slab medium, the integral can be written as:

$$\epsilon_{jm} = \frac{1}{a^2}\left(\epsilon_s \int_{\square} e^{-i\frac{2\pi}{a}(xj+ym)}da - (\epsilon_s-\epsilon_r) \int_{\bigcirc} e^{-i\frac{2\pi}{a}(xj+ym)}da\right). \tag{71}$$

The square integral is different from zero only when $n=0$ and $m=0$, and it is convenient to solve the circular integral in polar coordinates: $x = r'\cos\theta$, $y = r'\sin\theta$ and $da = r'dr'd\theta$. Thus:

$$\epsilon_{jm} = \epsilon_s\delta_{j0}\delta_{m0} - \frac{(\epsilon_s-\epsilon_r)}{a^2}\int_{\bigcirc} e^{-i\frac{2\pi r'}{a}(j\cos\theta+m\sin\theta)}r'dr'd\theta. \tag{72}$$

Using the following identities:

$$\begin{aligned}
&\int_0^{2\pi} e^{-ir'(A\cos\theta+B\sin\theta)}d\theta = 2\pi J_0\left(r'\sqrt{A^2+B^2}\right),\\
&\int_0^{r} r'J_0(Cr')dr' = r\frac{J_1(Cr)}{C},\\
&\lim_{C\to 0}\frac{J_1(Cr)}{C} = \frac{r}{2},
\end{aligned} \tag{73}$$

the ϵ_{jm} coefficients acquire the following closed form:

$$\epsilon_{jm} = \begin{cases} \epsilon_s + \frac{\pi(\epsilon_r-\epsilon_s)r^2}{a^2}, & j=0\wedge m=0\\ \frac{2\pi(\epsilon_r-\epsilon_s)r}{a^2}\frac{J_1\left(r\sqrt{\left(\frac{2\pi j}{a}\right)^2+\left(\frac{2\pi m}{a}\right)^2}\right)}{\sqrt{\left(\frac{2\pi j}{a}\right)^2+\left(\frac{2\pi m}{a}\right)^2}}, & j\neq 0\vee m\neq 0, \end{cases} \tag{74}$$

where J_l is the Bessel function of order l. The coefficients η_{jm}, associated to $\eta(x,y) = \frac{1}{\epsilon(x,y)}$, are obtained replacing ϵ_s and ϵ_r by $\frac{1}{\epsilon_s}$ and $\frac{1}{\epsilon_r}$ respectively in the expression (74).

A.2 HEXAGONAL LATTICE

The reciprocal lattice vector of the hexagonal lattice is:

$$\mathbf{G} = \frac{2\pi j}{a}\hat{\mathbf{x}} + \frac{2\pi}{a\sqrt{3}}(2m-j)\hat{\mathbf{y}}. \tag{75}$$

The expansion of the dielectric function in terms of a plane wave basis with the periodicity of the Bravais lattice is written as:

$$\epsilon(x,y) = \sum_{jm}\epsilon_{jm}e^{i\frac{2\pi}{a}(xj+y\frac{(2m-j)}{\sqrt{3}})}. \tag{76}$$

In the same way that it was made for the square lattice, $\epsilon(x,y)$ is multiplied by the function $e^{-i\frac{2\pi}{a}(xj'+y\frac{(2m'-j')}{\sqrt{3}})}$ and then integrated over the orthogonality region shown in Figure 27. Note that in this case such region does not correspond to the unit cell of the lattice.

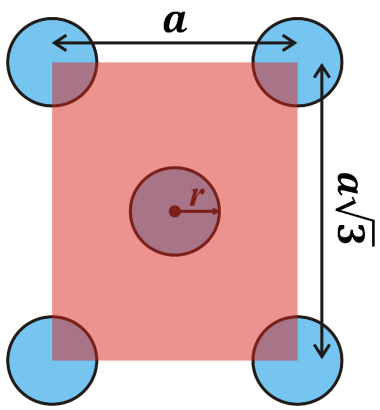

Figure 27: Integration region of the hexagonal lattice.

The coefficient is expressed as:

$$\epsilon_{jm} = \frac{1}{a^2\sqrt{3}} \int_{RO} \epsilon(x,y) e^{-i\frac{2\pi}{a}(xj+y\frac{(2m-j)}{\sqrt{3}})} da. \tag{77}$$

The integral is divided in two contributions, one corresponding to the rectangular region and the other one corresponding to the circular region:

$$\epsilon_{jm} = \epsilon_s \delta_{j0}\delta_{m0} - 2\frac{(\epsilon_s - \epsilon_r)}{a^2\sqrt{3}} \times \int_{\bigcirc} e^{-i\frac{2\pi r'}{a}(j\cos\theta + \frac{(2m-j)}{\sqrt{3}}\sin\theta)} r' dr' d\theta. \tag{78}$$

There is a factor of two in the circular integral since the total area contains two circles. Using the identities (73) the ϵ_{jm} coefficients take the closed form:

$$\epsilon_{jm} = \begin{cases} \epsilon_s + \frac{2\pi(\epsilon_r-\epsilon_s)r^2}{a^2\sqrt{3}} & , \ j = 0 \wedge m = 0 \\ \frac{4\pi(\epsilon_r-\epsilon_s)r}{a^2\sqrt{3}} \frac{J_1\left(r\sqrt{\left(\frac{2\pi j}{a}\right)^2 + \left(\frac{2\pi(2m-j)}{a\sqrt{3}}\right)^2}\right)}{\sqrt{\left(\frac{2\pi j}{a}\right)^2 + \left(\frac{2\pi(2m-j)}{a\sqrt{3}}\right)^2}} & , \ j \neq 0 \vee m \neq 0. \end{cases} \tag{79}$$

The coefficients η_{jm} associated to $\eta(x,y)$ are obtained replacing ϵ_s and ϵ_r by $\frac{1}{\epsilon_s}$ and $\frac{1}{\epsilon_r}$ respectively in the expression (79).

A.3 SUPERPOSITION OF DIELECTRIC FUNCTIONS: DEFECTIVE SUPERCELLS

The simplest way to model defective supercells is through the superposition of dielectric functions, one of these associated to the regular

non-defective crystal with lattice parameter a, and the other ones associated to the same crystal albeit with larger lattice parameter A (the superlattice parameter) which will determine the supercell defects. It is important to take into account that the superlattice vectors must be integer multiples of the regular lattice vectors (associated to the crystal with lattice parameter a). The basic case corresponds to the defect L1 or H1 (one cylinder or hole missing) whose dielectric function can be written as:

$$\epsilon^{L1}(x,y) = \epsilon(x,y) + \epsilon^{1}(x,y). \tag{80}$$

Here, $\epsilon(x,y)$ and $\epsilon^{1}(x,y)$ are the dielectric functions of the regular crystal with lattice parameters a and $A = la$ respectively, where l is an integer number. In the particular case of the square lattice $\epsilon^{L1}(x,y)$ is expanded as:

$$\epsilon^{L1}(x,y) = \sum_{jm} \epsilon_{jm} e^{i\frac{2\pi}{a}(xj+ym)} + \sum_{jm} \epsilon^{1}_{jm} e^{i\frac{2\pi}{la}(xj+ym)}. \tag{81}$$

Since the defective system has the periodicity of the supercell, the expression (81) is multiplied by a plane wave $e^{-i\frac{2\pi}{la}(xj'+ym')}$ with period A, and integrated over the orthogonality region of the basis, which is the supercell in this case:

$$\begin{aligned}(al)^2 \epsilon^{L1}_{j'm'} &= \int_{A_S} \epsilon^{L1}(x,y) e^{-i\frac{2\pi}{la}(xj'+ym')} da \\ &= \sum_{jm} \epsilon_{jm} \int_{A_S} e^{i\frac{2\pi}{a}(x(j-\frac{j'}{l})+y(m-\frac{m'}{l}))} da + \\ &\quad \sum_{jm} \epsilon^{1}_{jm} \int_{A_S} e^{i\frac{2\pi}{la}(x(j-j')+y(m-m'))} da.\end{aligned} \tag{82}$$

Solving the integrals of (82) it is obtained:

$$\begin{aligned}(al)^2 \epsilon^{L1}_{j'm'} = (al)^2 &\sum_{jm} \epsilon_{jm} \delta_{j',jl} \delta_{m',ml} + \\ (al)^2 &\sum_{jm} \epsilon^{1}_{jm} \delta_{j',j} \delta_{m',m}.\end{aligned} \tag{83}$$

Therefore, the closed expression for the expansion coefficients of the L1 defect is:

$$\epsilon^{L1}_{jm} = \epsilon_{\frac{j}{l},\frac{m}{l}} + \epsilon^{1}_{j,m}. \tag{84}$$

If $\frac{j}{l}$ or $\frac{m}{l}$ are not integers $\epsilon_{\frac{j}{l},\frac{m}{l}}$ vanishes. The expression (84) also applies to the hexagonal lattice. To ensure that ϵ^{L1}_{jm} will reproduce the L1 defect, the quantities ϵ_s, ϵ_r, ϵ^{1}_{s} and ϵ^{1}_{r} must be conveniently chosen in the expression (74) and (79):

$$\begin{aligned}\epsilon_s &= \epsilon^{S}_{s}, & \epsilon_r &= \epsilon^{S}_{r}, \\ \epsilon^{1}_{s} &= 0, & \epsilon^{1}_{r} &= \epsilon_s - \epsilon_r.\end{aligned} \tag{85}$$

ϵ_r^S and ϵ_s^S will correspond to the dielectric functions of the cylinder and the slab medium in the supercell respectively. The choices (85) ensure that when the dielectric functions are superposed the central cylinder vanishes without affecting the surrounding cylinders. In the same way, the L2 (two horizontal aligned missing holes) and L3 (three horizontal aligned missing holes) defects can be created through superpositions. The results for their respective coefficients are:

$$\epsilon_{jm}^{L2} = \left(\epsilon_{\frac{j}{l},\frac{m}{l}} + \epsilon_{j,m}^1 + \epsilon_{j,m}^1 e^{i\frac{2\pi j}{l}}\right) e^{-i\frac{\pi j}{la}}, \tag{86}$$

$$\epsilon_{jm}^{L3} = \epsilon_{\frac{j}{l},\frac{m}{l}} + \epsilon_{j,m}^1 + 2\epsilon_{j,m}^1 \cos\frac{2\pi j}{l}. \tag{87}$$

Because in the L2 defect one of the cylinders vanishes at $x = a$, the displacement of $\epsilon^1(x,y)$ generates a factor of $e^{i\frac{2\pi j}{l}}$ in the coefficient, furthermore, to center the defect in the supercell $\epsilon^{L2}(x,y)$ is displaced $0.5a$, producing a global factor of $e^{-i\frac{\pi j}{la}}$ in the coefficient ϵ_{jm}^{L2}. The cosine term in the L3 coefficient is the product of the simplification of two phases in $x = -a$ and $x = a$.

The L3 defect with an outward displacement of the two lateral cylinders is produced eliminating the lateral cylinders of the regular L3 defect (87), and then creating the two cylinders displaced. If the new centers of the displaced cylinders are located at $x = -(2+s)a$ and $x = (2+s)a$, the Fourier coefficients take the form:

$$\epsilon_{jm}^{L3-shift} = \epsilon_{\frac{j}{l},\frac{m}{l}} + \epsilon_{j,m}^1 + 2\epsilon_{j,m}^1 \cos\frac{2\pi j}{l} + 2\epsilon_{j,m}^1 \cos\frac{4\pi j}{l} + 2\epsilon_{j,m}^2 \cos\frac{2\pi j(2+s)}{l}. \tag{88}$$

$\epsilon_{j,m}^2$ are the coefficients of a superlattice with the same geometrical properties of the lattice generated by $\epsilon_{j,m}^1$, however with respective dielectric constants $\epsilon_r^2 = \epsilon_r - \epsilon_s$ and $\epsilon_s^2 = 0$.

The coefficients associated to the waveguides have no restriction over the j index, since the supercell has the same period of the regular crystal, with lattice parameter a, in the x direction:

$$\epsilon_{jm}^g = \epsilon_{j,\frac{m}{l}} + \epsilon_{j,m}^{Sg}, \tag{89}$$

where $\epsilon_{j,m}^{Sg}$ has the following closed form for the square lattice:

$$\epsilon_{jm}^{Sg} = \begin{cases} \epsilon_s^{Sg} + \frac{\pi(\epsilon_r^{Sg} - \epsilon_s^{Sg})r^2}{la^2} & , \ j = 0 \wedge m = 0 \\ \frac{2\pi(\epsilon_r^{Sg} - \epsilon_s^{Sg})r}{la^2} \frac{J_1\left(r\sqrt{\left(\frac{2\pi j}{a}\right)^2 + \left(\frac{2\pi m}{la}\right)^2}\right)}{\sqrt{\left(\frac{2\pi j}{a}\right)^2 + \left(\frac{2\pi m}{la}\right)^2}} & , \ j \neq 0 \vee m \neq 0. \end{cases} \tag{90}$$

And the following closed form for the hexagonal lattice:

$$\epsilon_{jm}^{Sg} = \begin{cases} \epsilon_s^{Sg} + \frac{2\pi(\epsilon_r^{Sg}-\epsilon_s^{Sg})r^2}{la^2\sqrt{3}} & , \; j = 0 \wedge m = 0 \\ \frac{4\pi(\epsilon_r^{Sg}-\epsilon_s^{Sg})r}{la^2\sqrt{3}} \frac{J_1\left(r\sqrt{\left(\frac{2\pi j}{a}\right)^2+\left(\frac{2\pi(2m-jl)}{la\sqrt{3}}\right)^2}\right)}{\sqrt{\left(\frac{2\pi j}{a}\right)^2+\left(\frac{2\pi(2m-jl)}{la\sqrt{3}}\right)^2}} & , \; j \neq 0 \vee m \neq 0. \end{cases} \tag{91}$$

For both waveguides, square and hexagonal, the respective dielectric constants of the superlattice are $\epsilon_s^{Sg} = 0$ and $\epsilon_r^{Sg} = \epsilon_s - \epsilon_r$.

Remember that the coefficients η_{jm} associated to $\eta(x,y)$ are obtained replacing ϵ_s and ϵ_r by $\frac{1}{\epsilon_s}$ and $\frac{1}{\epsilon_r}$ respectively, in the basic expressions (74) and (79).

B

THE L3 CAVITY

The realization of nano cavities with high quality factor Q and small modal volume V has become very important since the ratios Q/V, $Q/\sqrt{V}$ and Q^2/V characterize a wide range of phenomena in areas as nonlinear optics and cavity quantum electrodynamics (QED)[1]. Besides that, ultra small cavities enable large-scale integration in a single optical chip. Photonic crystals cavities are optimal candidates to fulfill these requirements; their light confinement mechanism, which consists in an extension of the Bragg reflection to two and three dimensions, is very efficient, allowing to reach very high Q and small V values. And multiple photonic crystal devices can be implemented in the same dielectric wafer, allowing large-scale integration.

The L3 nano cavity was the first photonic crystal cavity with experimental quality factors in the order of 45.000 and small modal volume (about 7.0×10^{-14} cm) [50]. It has been the subject of intense research for applications in control of ultrafast laser pulses [51], low-threshold lasing [6], cavity QED and single photon sources [52, 53]. The L3 cavity studied in this work consists of three missing horizontal holes in a two dimensional photonic crystal slab of a hexagonal lattice of holes. Figure 28 shows the L3 cavity where a is the lattice parameter. An additional outward displacement of the end lateral holes s is made to smooth the field in the cavity edges, producing a decrease of radiation losses and consequently an increase of the quality factor [50, 54].

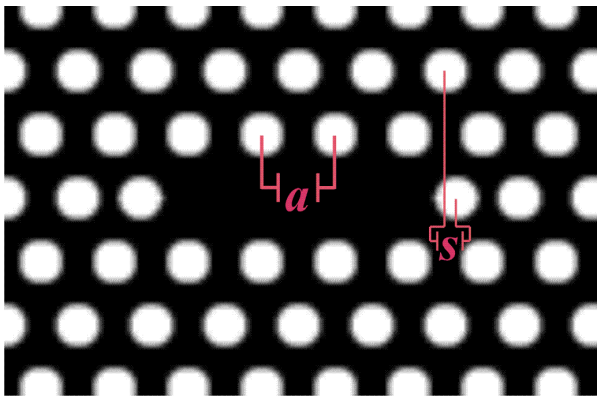

Figure 28: L3 cavity with lattice parameter a and an outward displacement s of the end lateral holes.

1 See Chapter 1.

The mode structure of the L3 cavity with $s = 0.15a$ is shown in Figure 29, there is plotted the time averaged electric field energy density distribution $\mathbf{E} \cdot \mathbf{D}$ superposed with the dielectric function of the crystal. The cavity supports six modes in the TE-like polarization symmetry[2] of the photonic crystal, which has a full TE-like band gap for refractive indexes $n \geqslant 1.6$ [54]. The frequencies ν, in units of c/a, are written above each mode. As it is expected, the fundamental mode has a strong field intensity in the center of the cavity, and usually, this is the most important state for practical applications. The calculations were made using a supercell of $12a \times 12a \times 4a$ with the free software package MPB, which computes the fully vectorial eigenmodes of Maxwell equations with periodic boundary conditions by preconditioned conjugate-gradient minimization of the block Rayleigh quotient in a plane wave basis [55]. The crystal parameters in the calculation were: hole radius $r = 0.29a$, slab thickness $d = 0.5a$, refractive index $n = 3.5$ and the spatial grid resolution was chosen to be 10 pixels by unit of a.

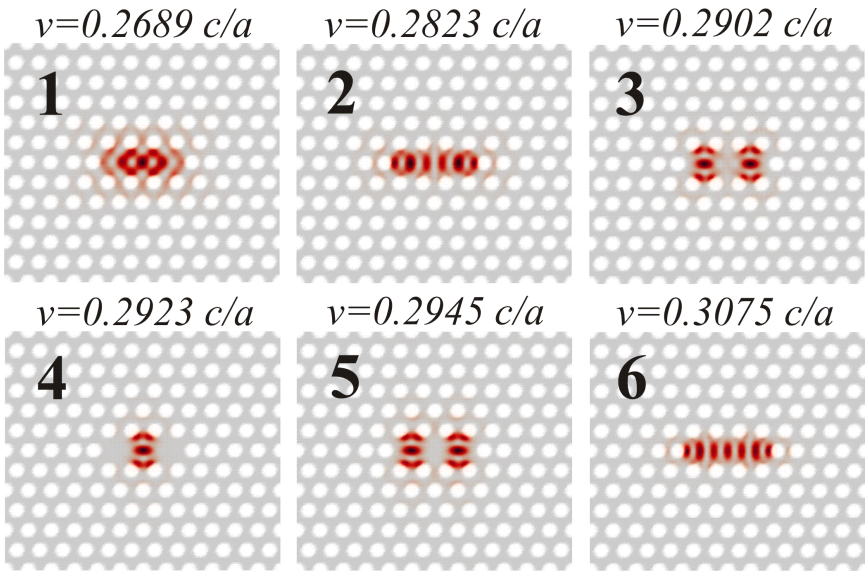

Figure 29: Time averaged electric field energy density $\mathbf{E} \cdot \mathbf{D}$ of the six L3 cavity modes. The frequency ν, written in units of c/a, is shown above of each mode.

To study the fundamental L3 cavity mode polarization, finite difference time domain (FDTD) simulations were made using the package MEEP [56] in a finite photonic crystal, Figure 30 shows the results obtained for the same cavity parameters of Figure 29. The mode has non-zero E_x and E_y components, which means that there is no pure polarizations in x or y directions, nevertheless, the y component is dominant as it can be seen in the vector field diagram of Figure 30. It

2 TE-like polarization is the extension of the TE case, studied in Chapter 3, to symmetric photonic crystal slabs. See reference [23].

is important to take into account this fact, because even though the most efficient way to excite the mode is through the y component, it is possible to excite it through the x component also[3]. The FDTD calculations were made on a crystal of size $16a \times 6\sqrt{3}a$, located inside a computational cell with a perfectly matched layer (PML) in the boundaries [57, 58]. The spacial grid resolution was chosen to be 20 pixels by lattice parameter and the time resolution is automatically fixed by the Courant condition [59]. This resolution produces a frequency value ν for the fundamental mode of 0.26926 c/a, which is located in the convergence region. The references [34, 60] can be consulted to obtain more details about the polarizations of the L3 cavity modes.

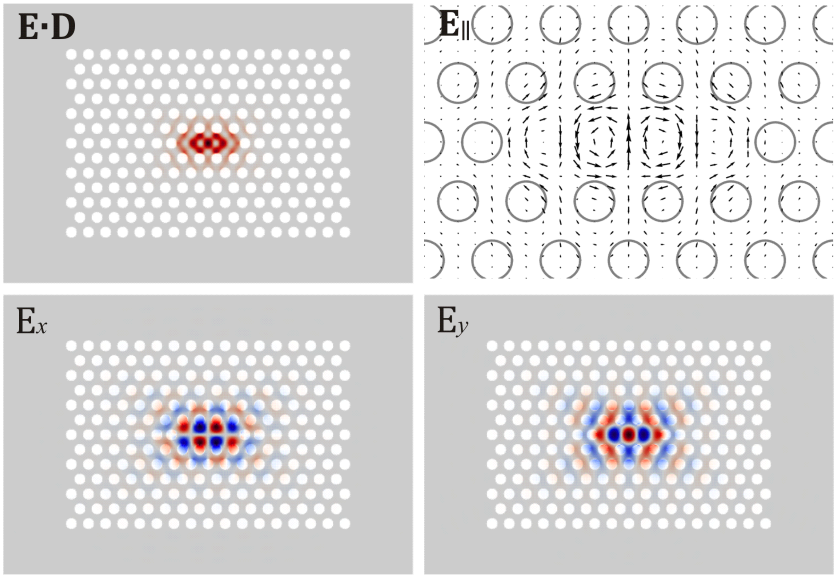

Figure 30: FDTD results for the energy and field distributions of the fundamental L3 cavity mode. (Top-left) Time averaged electric field energy density $\mathbf{E} \cdot \mathbf{D}$. (Top-right) In-plane electric field $\mathbf{E}_{||}$. (Bottom-left) x component distribution of the electric field E_x. (Bottom-right) y component distribution of the electric field E_y. Blue corresponds to minimum values and red to maximum values.

Figure 31 shows the behavior of the quality factor and the frequency in terms of the outward hole shift s for the fundamental mode. The FDTD simulations show that the quality factor attain a maximum value of 5×10^4 at $s = 0.2a$, which agrees with the literature [54], and the frequency mode undergoes a maximum change of 0.85% at $s = 0.225a$.

3 See Chapter 6.

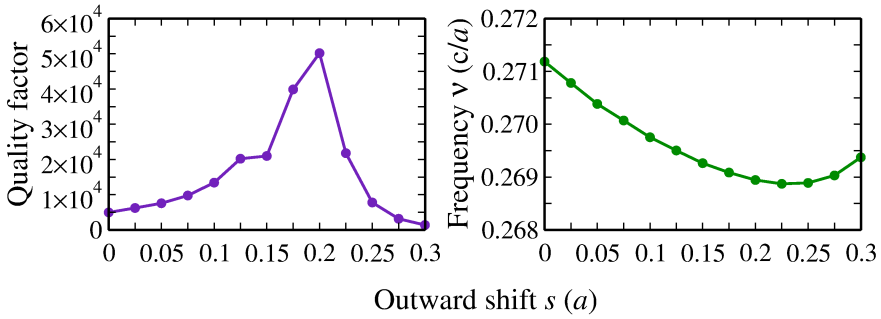

Figure 31: Q and frequency behavior in terms of the outward hole displacement s. The FDTD simulations were made with the same crystal parameters adopted in this appendix.

The software packages used to make the calculations of this appendix, can be freely downloaded in the following web sites:

http://ab-initio.mit.edu/mpb
http://ab-initio.mit.edu/meep

BIBLIOGRAPHY

[1] Rayleigh, "On the remarkable phenomenon of crystalline reflexion described by Prof. Stokes," *Phil. Mag*, vol. 26, pp. 256–265, 1888.

[2] V. P. Bykov, "Spontaneous emission from a medium with a band spectrum," *Quantum Electronics*, vol. 4, pp. 861–871, 1975.

[3] E. Yablonovitch, "Inhibited Spontaneous Emission in Solid-State Physics and Electronics," *Physical Review Letters*, vol. 58, pp. 2059–2062, 1987.

[4] S. John, "Strong localization of photons in certain disordered dielectric superlattices," *Physical Review Letters*, no. 58, pp. 2486–2489, 1987.

[5] K. J. Vahala, "Optical microcavities," *Nature*, vol. 424, no. 839.

[6] N. Masahiro, K. Tanabe, S. Iwamoto, and Y. Arakawa, "High-Q design of semiconductor-based ultrasmall photonic crystal nanocavity," *Optics Express*, vol. 18, no. 8, pp. 8144–8150, 2010.

[7] K. Yao and Y. Shi, "High-Q width modelated photonic crystal stack mode-gap cavity and its application to refractive index sensing," *Optics Express*, vol. 20, no. 24, pp. 27039–27044, 2012.

[8] S. Mingaleev and Y. Kivshar, "Nonlinear Photonic Crystals Toward All-Optical Technologies," *Optics and Photonics News*, vol. 13, no. 7, pp. 48–51, 2002.

[9] J. Bravo-Abad, A. Rodriguez, P. Bermel, S. G. Johnson, J. D. Joannopoulos, and M. Soljacic, "Enhanced nonlinear optics in photonic-crystal microcavities," *Optics Express*, vol. 15, no. 24, pp. 16161–16176, 2007.

[10] V. Berger, "Nonlinear Photonic Crystals," *Physical Review Letters*, vol. 81, no. 19, pp. 4136–4139, 1998.

[11] K. Nozaki, T. Tanable, A. Shinya, S. Matsuo, T. Sato, H. Taniyama, and M. Notomi, "Sub-femtojoule all-optical switching using a photonic-crystal nanocavity," *Nature Photonics*, vol. 4, pp. 477–483, 2010.

[12] M. F. Yanik, S. Fan, M. Soljacic, and J. D. Joannopoulos, "All-optical transistor action with bistable switching in a photonic crystal cross-waveguide geometry," *Optics Letters*, vol. 28, no. 24, pp. 2506–2508, 2003.

[13] Y. Liu, F. Qin, Z.-M. Meng, F. Zhou, Q.-H. Mao, and Z.-Y. Li, "All-optical logic gates based on two-dimensional low-refractive-index nonlinear photonic crystal slabs," *Optics Express*, vol. 19, no. 3, pp. 1945–1953, 2011.

[14] X. Yang, C. Husko, C. W. Wong, M. Yu, and D.-L. Kwong, "Observation of femtojoule optical bistability involving Fano resonances in high-Q/V silicon photonic crystal nanocavities," *Applied Physics Letters*, vol. 91, no. 051113, 2007.

[15] W. Ding, B. Luk'yanchuk, and C.-W. Qiu, "Ultrahigh-contrast-ratio silicon Fano diode," *Physical Review A*, vol. 85, no. 025806, 2012.

[16] J. wang, X. Chen, Z. Li, and W. Lu, "Study of grating performance for quantum well photodetectors ," *Journal of the optical society of america B*, vol. 27, no. 117401, pp. 2428–2432, 2010.

[17] Y. Zhang, H. Chen, Z. Li, N. Li, X. Chen, and W. Lu, "The optical coupling improvement of THz quantum well infrared photodetectors based on the plasmonic induced near-field effect," *Physica B*, vol. 405, pp. 552–554, 2010.

[18] S. Kalchmair, R. Gansch, S. Ahn, A. Andrews, H. Detz, T. Zederbauer, E. Mujagic, P. Reininger, G. Lasser, W.Schrenk, and G. Strasser, "Detectivity enhancement in quantum well infrared photodetectors utilizing a photonic crystal slab resonator," *Optics Express*, vol. 20, no. 58, pp. 5622–5628, 2012.

[19] N. W. Ashcroft and N. D. Mermin, *Solid State Physics*. Brooks Cole, first ed., 1976.

[20] M. Skorobogativ and J. Yang, *Fundamentals of Photonic Crystal Guiding*. Camdridge University Press, first ed., 2009.

[21] J. D. Jackson, *Classical Electrodynamics*. Wiley, third ed., 1998.

[22] J. Sakurai, *Modern Quantum Mechanics*. Addison Wesley, revised ed., 1993.

[23] J. D. Joannopoulos, S. G. Johnson, and J. N. Winn, *Photonic Crystals: Molding the Flow of Light*. Princenton University Press, second ed., 2008.

[24] K. Sakoda, *Optical Properties of Photonic Crystals*. Springer, second ed., 2004.

[25] L. C. Andreani and D. Gerace, "Photonic-crystal slabs with a triangular lattice of triangular holes investigated using a guided-mode expansion method," *Physical Review B*, vol. 73, no. 235114, 2006.

[26] K. Ho, C. Chan, and C. Soukoulis, "Existence of a Photonic Gap in Periodic Dielectric Structures," *Physical Review Letters*, vol. 65, pp. 3152–3155, 1990.

[27] H. Sozuer and J. Haus, "Photonic bands: Convergence problems with the plane-wave method," *Physical Review B*, vol. 45, pp. 13962–13972, 1992.

[28] J. D. Shumpert, *Modeling of Periodic Dielectric Structures (Electromagnetic Crystals)*. PhD thesis, University of Michigan, 2001.

[29] G. Tayeb and D. Maystre, "Rigorous theoretical study of finite-size two-dimensional photonic crystals doped by microcavities ," *Journal of the optical society of america A*, vol. 14, no. 12, pp. 3323–3332, 1997.

[30] L. Wu, F. Zhuang, and S. He, "Degeneracy analysis for a supercell of a photonic crystal and its application to the creation of band gaps," *Physical Review E*, vol. 67, no. 026612, 2003.

[31] J. Vasco and H. V. Posada, "Defective Mode Study For Photonic Crystals Through Plane Wave Expansion Method ," *Revista Colombiana de Física*, vol. 43, no. 3, pp. 846–855, 2011.

[32] J. Yonekura, M. Ikeda, and T. Baba, "Analysis of Finite 2-D Photonic Crystals of Columns and Lightwave Devices Using the Scattering Matrix Method ," *Journal of lightwave technology*, vol. 17, no. 8, pp. 1500–1508, 1999.

[33] E. Centeno and D. Felbacq, "Rigorous vector diffraction of electromagnetic waves by bidimensional photonic crystals ," *Journal of the optical society of america A*, vol. 17, no. 2, pp. 320–327, 2000.

[34] D. Whittaker and I. Culshaw, "Scattering-matrix treatment of patterned multilayer photonic structures," *Physical Review B*, vol. 60, pp. 2610–2618, 1999.

[35] D. Y. K. Ko and J. Inkson, "Matrix method for tunneling in heterostructures: Resonant tunneling in multilayer systems," *Physical Review B*, vol. 38, pp. 9945–9951, 1988.

[36] Z.-Y. Li and L.-L. Lin, "Photonic band structures solved by a plane-wave-based transfer-matrix method," *Physical Review E*, vol. 67, no. 046607, 2003.

[37] S. G. Johnson, S. Fan, P. R. Villeneuve, and J. Joannopoulos, "Guided modes in photonic crystal slabs ," *Physical Review B*, vol. 60, no. 8, pp. 5751–5758, 1999.

[38] D. Englund, A. Faraon, I. Fushman, N. Stoltz, P. Petroff, and J. Vuckovic, "Controlling cavity reflectivity with a single quantum dot," *Nature*, vol. 450, pp. 857–861, 2007.

[39] S. Fan and J. Joannopoulos, "Analysis of guided resonances in photonic crystals slabs," *Physical Review B*, vol. 65, no. 235112, 2002.

[40] U. Fano, "Effects of Configuration Interaction on Intensities and Phase Shifts," *Physical Review*, vol. 124, pp. 1866–1878, 1961.

[41] V. N. Astratov, I. S. Culshaw, R. M. Stevenson, D. M. Whittaker, M. S. Skolnick, T. F. Krauss, and R. M. D. L. Rue, "Resonant Coupling of Near-Infrared Radiation to Photonic Band Structure Waveguides ," *Journal of lightwave technology*, vol. 17, no. 117401, pp. 2050–2057, 1999.

[42] E. Driessen, D. Stolwijk, and M. de Dood, "Asymmetry reversal in the reflection from a two-dimensional photonic crystal," *Optics Letters*, vol. 32, no. 21, pp. 3137–3139, 2007.

[43] L. Babic and M. de Dood, "Interpretation of Fano lineshape reversal in the reflectivity spectra of photonic crystals slabs," *Optics Express*, vol. 18, no. 25, pp. 26569–26582, 2010.

[44] S. Fan, "Sharp asymmetric line shapes in side-coupled waveguide-cavity systems ," *Applied Physics Letters*, vol. 80, no. 6, pp. 908–910, 2002.

[45] N. Ou, J. Shyu, H. Lee, and J. Wu, "Diameter-dependent guided resonance of dielectric hole-array membrane ," *Journal of Vacuum Science and Technology B*, vol. 27, no. 6, pp. 3183–3186, 2009.

[46] A. E. Miroshnichenko, S. Flach, and Y. S. Kivshar, "Fano resonances in nanoscale structures," *Reviews of Modern Physics*, vol. 82, pp. 2257–2298, 2010.

[47] M. Galli, S. Portalupi, M. Belotti, L. Andreani, L. O'Faolain, and T. Krauss, "Light scattering and Fano resonances in high-Q photonic crystal nanocavities," *Applied Physics Letters*, vol. 94, no. 071101, 2009.

[48] Y. S. Joe, A. M. Satanin, and C. S. Kim, "Classical analogy of Fano resonances ," *Physica Scripta*, vol. 74, no. 259, pp. 259–266, 2006.

[49] P. Valentim, J. Vasco, I. Luxmoore, D. Szymanski, H. V. Posada, A. Fox, D. Whittaker, M. Skolnick, and P. Guimarães, "Asymmetry tuning of Fano resonances in GaAs photonic crystal cavities," *To be published*.

[50] Y. Akahane, T. Asano, B.-S. Song, and S. Noda, "High-Q photonic nanocavity in a two-dimensional photonic crystal," *Nature*, vol. 425, pp. 944–947, 2003.

[51] T. Asano, W. Kunishi, B.-S. Song, and S. Noda, "Time-domain response of point-defect cavities in two-dimensional photonic crystal slabs using picosecond light pulse ," *Applied Physics Letters*, vol. 88, no. 151102, 2006.

[52] W.-H. Chang, W.-Y. Chen, H.-S. Chang, T.-P. Hsieh, J.-I. Chyi, and T.-M. Hsu, "Efficient Single-Photon Sources Based on Low-Density Quantum Dots in Photonic-Crystal Nanocavities ," *Physical Review Letters*, vol. 96, no. 117401, p. 4, 2006.

[53] A. Schwagmann, S. Kalliakos, D. J. Ellis, I. Farrer, J. P. Griffiths, G. A. Jones, D. A. Ritchie, and A. J. Shields, "In-plane single-photon emission from a L3 cavity coupled to a photonic crystal waveguide ," *Optics Express*, vol. 20, no. 27, pp. 28614–28624, 2012.

[54] A. Adawi, A. Chalcraft, D. Whittaker, and D. Lidzey, "Refractive index dependence of L3 photonic crystal nano-cavities ," *Optics Express*, vol. 15, no. 22, pp. 14299–14305, 2007.

[55] S. G. Johnson and J. Joannopoulos, "Block-iterative frequency-domain methods for Maxwell's equations in a planewave basis," *Optics Express*, vol. 8, no. 3, pp. 173–190, 2001.

[56] A. F. Oskooi, D. Roundy, M. Ibanescu, P. Bermel, J. Joannopoulos, and S. G. Johnson, "MEEP: A flexible free-software package for electromagnetic simulations by the FDTD method," *Computer Physics Communications*, vol. 181, pp. 687–702, 2009.

[57] J. Fang and Z. Wu, "Generalized Perfectly Matched Layer for the Absorption of Propagating and Evanescent Waves in Lossless and Lossy Media," *IEEE Transactions on Microwave Theory and Techniques*, vol. 44, no. 12, pp. 2216–2222, 1996.

[58] E. A. Marengo, C. M. Rappaport, and E. L. Miller, "Optimum PML ABC Conductivity Profile in FDFD," *IEEE Transactions on Magnetics*, vol. 35, no. 3, pp. 1506–1509, 1999.

[59] A. Taflove and S. C. Hagness, *Computational Electrodynamics: The Finite-Difference Time-Domain Method*. Atech House Publishers, third ed., 2005.

[60] R. Oulton, B. Jones, S. Lam, A. Chalcraft, D. Szymanski, D. O'Brien, T. Krauss, D. Sanvitto, A. Fox, D. Whittaker, M. Hopkinson, and M. Skolnick, "Polarized quantum dot emission from photonic crystal nanocavities studied under mode-resonant enhanced excitation ," *Optics Express*, vol. 15, no. 25, pp. 17221–17230, 2007.

COLOPHON

This document was typeset using the typographical look-and-feel `classicthesis` developed by André Miede. The style was inspired by Robert Bringhurst's seminal book on typography "*The Elements of Typographic Style*". `classicthesis` is available for both LaTeX and LyX:

http://code.google.com/p/classicthesis/